nature communications

Article

https://doi.org/10.1038/s41467-026-75101-w

High-rate single-crystalline Li-rich layered oxide with diversified surface-phase cation ordering for Li-ion batteries

Received: 9 August 2025

Accepted: 18 June 2026

Published online: 01 July 2026

Check for updates

Jingxi Zhang[1], Shile Chen[1], Yuting Xia[1], Ye Xiao[1], Meicen Fan[1], Rong-Ao Tong[1], Zehui Liu[1], Zhuoran Lv[2], Yaqi Liao[3], Moonsu Yoon[4], Mengyuan Zhou[3], Yanhao Dong[1] ✉, Ju Li[5,6] ✉ & Chang-An Wang[1] ✉

Advanced lithium-ion batteries require fast-charging high-energy-density electrodes. Li- and Mn-rich layered positive electrodes can offer higher capacity (>280 mAh g^{-1}) and higher specific energy (>1000 Wh kg^{-1}) than Ni-rich chemistries, yet it is challenging to produce volumetric-energy-dense Li-rich single crystals. Another concern is the rate performance. Li-rich layered oxides have long been considered to have poor rate capability, not to mention their single-crystal version. Here we report high-rate single-crystal Li-rich layered oxides with fast rechargeability. 0.2 C-discharge capacity of 248 mAh g^{-1}at 5 C fast-charging as well as 5 C fast-discharging capacity of 179 mAh g^{-1} are demonstrated. We prove that the fast rechargeability can be resolved by a complex cation ordering of coherent layered-, cation mixed-, rock salt-, and spinel-type structure. The highly conductive and electrochemically active surface phases can buffer Li^+ concentration gradients and enable deeper bulk lithiation. The single-crystal morphology and redesigned surface phase ensure mechanical and structural stability over cycling, improving capacity retention to 94.5% over 150 cycles at 0.5 C-rate. This work uncovers the intrinsic high-rate performance of single-crystal Li-rich layered oxides and calls attention to think about the fast-charging potential of positive electrodes with coarse microstructure.

Future development of lithium-ion battery (LIB) technology calls for fast-charging capability for portable electronics, electric vehicles, and integrated photovoltaic–energy storage systems[1,2]. Such demanding rate capability should come at a minimal cost to energy density and cycle life, in order to ensure balanced battery performance[3,4]. On the positive electrode side, Li- and Mn-rich layered oxides (LMRs) are promising candidate for post-nickel-rich chemistry, with reversible discharge capacity above 280 mAh g^{-1} and specific energy above 1000 Wh kg^{-1} [5–7]. In terms of positive electrode chemistry, microstructure, and electrochemistry, there are three points of consensus. First, it is challenging to synthesize kinetically favorable LMRs[8,9]. In the Ni-Co-Mn ternary space of layered oxides, Ni is capable of enhancing capacity and energy density, Co is capable to stabilize layered structure, electronic conduction and rate capability, while Mn is usually

[1]State Key Laboratory of New Ceramic Materials, School of Materials Science and Engineering, Tsinghua University, Beijing, China. [2]State Key Lab of Metal Matrix Composites, School of Materials Science and Engineering, Shanghai Jiao Tong University, Shanghai, China. [3]State Key Laboratory of Material Processing and Die and Mold Technology, School of Materials Science and Engineering, Huazhong University of Science and Technology, Wuhan, China. [4]Department of Chemical and Biological Engineering, Gachon University, Seongnam-si, Republic of Korea. [5]Department of Nuclear Science and Engineering, Massachusetts Institute of Technology, Cambridge, MA, USA. [6]Department of Materials Science and Engineering, Massachusetts Institute of Technology, Cambridge, MA, USA. ✉e-mail: dongyanhao@tsinghua.edu.cn; liju@mit.edu; wangca@tsinghua.edu.cn

added to enhance structural and thermal stability[10–14]. Mn-rich and Co-lean LMRs have been reported to have worse kinetics than $LiCoO_2$ and Ni-rich oxides, which has been attributed to poor electronic conductivity and sluggish anionic redox accompanied by transition metal migration[15,16]. As a result, LMRs are usually not preferred for high-rate applications.

Second, it is challenging to synthesize high-rate single-crystal positive electrodes. The main advantages of single-crystal materials (referring to micron-size primary particles without assembled secondary particle morphology in the battery field) are manifold. Compared with polycrystalline ones, single-crystal materials show better mechanical properties, enabling resistance to particle fracture during the calendaring process and thereby offering denser particle packing, higher electrode density, and higher volumetric energy density[17]. Commercial single-crystal $LiCoO_2$ can achieve electrode density as high as 4.1–4.2 g cm^{-3}, corresponding to >80% of the theoretical density of the crystal[18]. They also demonstrate good cycling stability owing to their lower specific surface area and higher resistance to cracking, which minimizes side-reaction-induced degradation processes such as gassing, transition-metal dissolution, and overgrowth of positive electrode–electrolyte interphases[19–21]. However, by definition, single crystals have no grain boundaries inside and the ambipolar diffusion of lithium ions and electrons proceeds through the lattice along the radial direction[17]. Therefore, they are expected to give worse rate performance than polycrystalline ones that have fine primary particle size and abundant grain boundaries that facilitate short-circuit diffusion[22–24]. In addition, owing to their much lower specific surface area and irregular morphologies rather than spherical agglomerates, conventional physical coating approaches suitable for polycrystalline materials may be ineffective for single-crystal materials[25].

Third, it is challenging to grow LMR single crystal. Driven by the advantages of single-crystal materials and the demonstrated success of single-crystal $LiCoO_2$ and single-crystal medium-Ni oxides, rapid progress has been achieved in producing single-crystal Ni-rich oxides in the past decade[26–28]. However, the reports on single-crystal LMR are rather limited. The present LMR technology follows the established methodology of precursor co-precipitation followed by heat treatment, originally developed for Ni-rich oxides. Yet the growth of primary particles and the elimination of secondary particle morphology require very high annealing temperatures and often degrade the electrochemical performance[16,29,30]. Among the few successful attempts in producing single-crystal LMR with satisfactory electrochemical performance, the majority rely on molten-salt or ion-exchange synthesis routes, which are considerably more difficult to scale up[31–35]. The fundamental mechanism underlying the difficulty of single-crystal LMR production is not clear at this stage. As a hypothesis, it may be attributed to the strong *d-p* hybridization between high-valence $Mn^{4+}$and O^{2-}, which suppresses mass transport rate-limiting oxygen ion diffusion and thereby inhibits particle coarsening during high-temperature synthesis.

Here we report progress in producing high-rate single-crystal LMR (H-SCLMR) overcoming the above three challenges. Single-crystal growth was promoted by planetary centrifugal deagglomeration[20] and slight lithium under-stoichiometry. For rate performance, we proposed that the previously unsatisfactory results were mainly limited by the surface rather than the bulk, and utilized an ammonium salt-leaching treatment for achieving a diverse cation ordering at the surface containing coherent layered-, cation mixed-, rock salt-, and spinel-type structure[36,37]. The surface phases are Li^+ ion conductive and electrochemically active, which can buffer Li^+ concentration gradients and enable deeper bulk lithiation. The synthesized micron-size single-crystal $Li_{1.2}Mn_{0.48}Ni_{0.16}Co_{0.16}O_2$ can deliver 286 mAh g^{-1} discharge capacity and 1040 Wh kg^{-1} specific energy (based on the positive electrode material) at 0.1 C (1 C defined as 250 mA g^{-1}), and very good rate performance (e.g., 197 mAh g^{-1} at 3 C/3 C charge-discharge and 179 mAh g^{-1} at 5 C/5 C charge-discharge). Fast charging capability higher than the polycrystalline control samples has been demonstrated: At 5 C fast-charging, the 0.2 C discharge capacity and specific energy are 248 mAh g^{-1} and 860 Wh kg^{-1} (based on the positive electrode material), corresponding to 86.7% retention in capacity and 82.7% retention in specific energy of 0.1 C/0.1 C charge/discharge, respectively. For rechargeability, 94.5% capacity retention is achieved over 150 cycles by effective suppression of oxygen evolution and internal strain[38–40]. Our work proves the surface bottleneck largely limits the rate performance of single-crystal LMR and the intrinsic kinetic advantages can be approached by renovated synthesis and surface design.

Results

In LMRs, the layered structure with Li_2MnO_3-type honeycomb ordering offers high capacity due to excess lithium and active oxygen redox[15]. Yet the labile oxygen with Li-O-Li coordination is easy to become volatile so the layered structure should only be used in the lattice but not at the surface[41]. In addition, loss of oxygen at the surface will result in uncontrollable growth of cation disordering and formation of rock-salt phase, which may further inhibit surface kinetics[42]. Thus, precise surface structural design is required. We propose that a diversified cation ordering within an O3-stacked oxygen framework (fcc close-packed stacking) can improve the electrochemical performance, especially under high-rate conditions. It has been reported that disordered rock-salt and $LiMn_2O_4$-type surface structures—which share the same O3-type oxygen stacking with layered structure—could effectively enhance the kinetics and stability of layered oxides[37,43]. In particular, it has been reported that a surface spinel structure is key to promoting capacity and inhibiting oxygen release in polycrystalline LMRs[37]. Regardless of its effectiveness, however, reports on surface structural design of single-crystal LMR are somehow limited, possibly due to the difficulty in single crystal synthesis.

In view of the transport, $LiMn_2O_4$-type spinel structure offers three-dimensionally connected Li^+ diffusion channels and electron polaron hopping network[44,45]. In view of the stability, lithium-deficient rock-salt-type structure is preferred due to electrochemical inactivity and strong metal-oxygen bonding[43,46,47]. Therefore, both structures are helpful. To coherently bridge the layered-type structure in the lattice and the rock salt-/spinel-type structure at the surface, cation-mixed structure can buffer interfacial stress and mitigate atomically abrupt phase boundaries. In short, complex cation ordering containing coherent layered-, cation mixed-, rock salt-, and spinel-type structures is sought. Such a complex ordering may only be produced under non-equilibrium conditions at relatively low temperatures, as the Gibbs phase rule excludes the coexistence of four phases.

For construction of H-SCLMR, we start with synthesizing single-crystal LMR (SCLMR). We synthesized the SCLMR using our previously reported planetary centrifugal deagglomeration method and a Li-to-transition-metal ratio (Li/*M*, *M* = Mn, Ni, and Co; in this work, $M = Mn_{0.6}Ni_{0.2}Co_{0.2}$) of 1.48[20]. The Li/*M* value was chosen because lithium under-stoichiometry is associated with sluggish growth kinetics. For example, Li/M = 1.35 yields a relatively high capacity but a small particle size (<200 nm) after high-temperature heat treatment. (Supplementary Fig. S1). On the other hand, lithium over-stoichiometry (Li/*M* = 1.55) promotes particle growth, but lowers the capacity (Supplementary Fig. S2) due to large agglomerations. After a fine screening among Li/*M* from 1.35 to 1.55 (Supplementary Figs. S1–S3), Li/*M* = 1.48 was chosen for its balance between single-crystal particle size and electrochemical performance. The obtained SCLMR is confirmed to have a layered structure matching the phase of LMR by synchrotron X-ray diffraction (SXRD), as shown in Supplementary Fig. S4a and Supplementary Table S1. The average particle size is around 1 μm (SEM image and particle size distribution are shown in Supplementary Fig. S4b). For comparison, the average diameters of the primary and

secondary particles of PCLMR are 0.23 and 7.4 μm, respectively (Supplementary Fig. S5).

To realize the diversified surface design, an $(NH_4)_2SO_4$-assisted leaching method was proposed to control the surface composition, followed by a 300 °C annealing process to achieve a non-equilibrium phase distribution[36]. The transformation process can be rationalized in three sequential steps:

(a) Li^+ elimination: In the near-surface region, lithium ions are partially leached by the $(NH_4)_2SO_4$ treatment, leading to a delithiated layered structure.

(b) Transition-metal migration: The resulting charge imbalance drives the migration of transition-metal ions from the transition-metal layer into the lithium layer. As this reconstruction proceeds via a topotactic and in situ mechanism, the resulting surface structure remains highly coherent with the underlying single-crystal bulk.

(c) Formation of the diversified structure: The limited thermal driving force provided by low-temperature annealing cannot complete the transformation into a fully crystallized thermodynamically favored spinel phase. Consequently, a non-equilibrium, diversified mosaic structure is stabilized at the surface.

Lithium deficiency in the final product H-SCLMR was characterized by inductively coupled plasma optical emission spectrometer (ICP-OES, Supplementary Table S2). The optimal amount of $(NH_4)_2SO_4$ was identified as 5 wt% of SCLMR (Supplementary Fig. S6). Surface area measurement reveals few specific surface area change during after modification (Supplementary Table S3).

Figure 1a shows the morphology of H-SCLMR, which is similar to that of SCLMR and exhibits an average particle size of approximately 1 μm. No obvious morphological changes were observed after the surface treatment. Energy-dispersive spectroscopy (EDS) mapping in Fig. 1b confirms the uniform distribution of Mn, Ni, and Co within the single-crystal particle. High-resolution SXRD and Rietveld refinement analysis in Fig. 1c (refinement parameters shown in Supplementary Table S4) show that H-SCLMR has a phase composition of 98.52% layered phases ($R-3m$ and $C/2m$) and 1.48% "spinel" phase (attributed to the lithium-deficient surface); further increasing the amount of $(NH_4)_2SO_4$ in the treatment would increase the content of the "spinel" phase, as shown in Supplementary Fig. S7. Supplementary Note 1 discusses the necessity of introducing a spinel phase in refinement. Here, we note that the SXRD data reveal the low-crystalline nature of the secondary phases by identifying widened signals in the 300 °C-annealed sample, whereas additional signals with sharper peaks in the 800 °C-annealed sample can be directly indexed to the crystallized spinel phase (Supplementary Fig. S8).

Surface-sensitive characterizations were conducted to understand the surface structure. Aberration-corrected high-angle annular dark-field (HAADF) scanning transmission electron microscope (STEM) image reveals that the surface of the control group (SCLMR) shows an integral layered phase (Fig. 1d). Raman spectroscopy was conducted to characterize the surface phases. Compared to SCLMR, H-SCLMR shows a shoulder peak at 625 cm^{-1} (Fig. 1e), which is more clearly observed in the differential spectrum. This shoulder peak is attributed to A_{1g} vibration in the Li-poor LiM_2O_4 phase[48]. Mn L_3-edge soft X-ray absorption spectra (sXAS) collected using the total electron yield (TEY) mode are highly sensitive to the surface valence state. The results for SCLMR and H-SCLMR at pristine and fully discharged states demonstrate an activated surface $Mn^{4+}\rightarrow Mn^{3+}$ redox transition in H-SCLMR, indicating the presence of spinel-related surface phases with overlithiation activity (Fig. 1f)[45].

Aberration-corrected HAADF-STEM was used to further investigate the bulk structure (Supplementary Fig. S9) and surface structure (Fig. 1g) of H-SCLMR along the (100) axis of the layered lattice ($R-3m$ phase). The bulk image in Supplementary Fig. S9 shows a conventional layered structure. The surface structure image in Fig. 1g shows the coexistence of diverse atomic structures with different cation ordering characteristics, including Li-rich (i.e., Li/$M>1$) layered structure in Fig. 1h, Li-poor (i.e., Li/$M<1$) spinel structure in Fig. 1i, Li-poor rock salt structure in Fig. 1j and Li-poor Li/M cation mixed structure in Fig. 1k. Such diversified structures were verified across various particles and projections (Supplementary Fig. S10). The cation-mixed structure should have intermediate Li content and electrochemical activity between the layered structure and the rock-salt/spinel structures, thus serving as a bonding layer to buffer stresses during electrochemical cycling. The four identified characteristic cation ordering coexist within the same O3-stacked oxygen ion framework with high coherency. We note the similarity between the complex surface phases of H-SCLMR and the recently reported partially disordered spinel-rock salt structure that shows ultrahigh rate performance and structural stability[44,49]. Such a diversified surface structure is expected to enhance structural integrity, rate performance and electrochemical stability in a balanced way.

We next evaluated the electrochemical properties of H-SCLMR in half-cells using Li metal negative electrode and commercial carbonate electrolytes. In the formation cycle at 0.1 C between 2.0 V and 4.8 V (vs. Li^+/Li), H-SCLMR shows a discharge capacity of 286 mAh g^{-1}, Coulombic efficiency (CE) of 83.4%, and discharge specific energy of 1040 Wh kg^{-1} (Fig. 2a, based on the positive electrode material). In comparison, SCLMR without surface treatment has 252 mAh g^{-1} capacity, 74.3% first-cycle CE, and 919 Wh kg^{-1} specific energy (based on the positive electrode material), and polycrystalline LMR (PCLMR) synthesized using the same precursors has 256 mAh g^{-1} capacity, 74.5% CE, and 939 Wh kg^{-1} specific energy (based on the positive electrode material). The improved capacity, CE, and specific energy of H-SCLMR can be attributed to the stabilized surface and higher first-cycle CE as all three samples have similar charge capacities in the formation cycle. The rate tests were next conducted and the rate performance of H-SCLMR, SCLMR, and PCLMR are compared in Fig. 2b. While SCLMR shows worse rate capability than PCLMR, H-SCLMR shows significant improvement over the former two. The discharge capacity of H-SCLMR under constant-current (CC) 3 C/3 C charge/discharge condition between 2.0-4.8 V (vs. Li^+/Li) and without constant-voltage (CV) holding is 197 mAh g^{-1}, corresponding to 72.0% capacity retention with respect to that at 0.3 C/0.3 C. At 5 C/5 C, H-SCLMR has a discharge capacity of 179 mAh g^{-1}, corresponding to 65.4% capacity retention. In comparison, SCLMR has discharge capacity of 157 mAh g^{-1} (67.8% capacity retention) and 141 mAh g^{-1} (60.7% capacity retention) at 3 C/3 C and 5 C/5 C, respectively. PCLMR has discharge capacity of 180 mAh g^{-1} and 155 mAh g^{-1} at 3 C/3 C and 5 C/5 C, respectively. The high-rate capability of H-SCLMR can be further demonstrated by the fast-charging experiments in Fig. 2c. Here we conducted CC nC/0.2 C charge/discharge between 2.0-4.8 V (vs. Li^+/Li), where n increases from 0.3 to 5. At 0.3 C/0.2 C, H-SCLMR has a discharge capacity of 279 mAh g^{-1}. Under fast-charging, H-SCLMR has remarkably high discharge capacities of 255 mAh g^{-1} and 248 mAh g^{-1} at 3 C/0.2 C and 5 C/0.2 C, corresponding to capacity retentions of 91% and 89% with respect to that at 0.3 C/0.2 C, respectively. We note that a metastable, diversified surface cation ordering is more effective in enhancing kinetic properties than a thermodynamically stable spinel phase, as the kinetic performance of H-SCLMR becomes worse after high-temperature (500 °C and 800 °C) annealing (Supplementary Fig. S8c and d).

To clarify the origin of the high-rate capability, we conducted galvanostatic intermittent titration technique (GITT) tests on all three samples. The Li^0 diffusion coefficient D_{Li} calculated from GITT measurements are plotted in Fig. 2d. The lowest D_{Li} is identified at the end of the charge and discharge, and H-SCLMR shows higher D_{Li} than SCLMR and PCLMR. It is interesting to note that D_{Li} of H-SCLMR at the end of the discharge does not show a monotonic decrease, as is the case for SCLMR and PCLMR. Instead, it first increases by more than two orders of magnitude and then decreases at the last GITT step). This is

https://doi.org/10.1038/s41467-026-75101-w

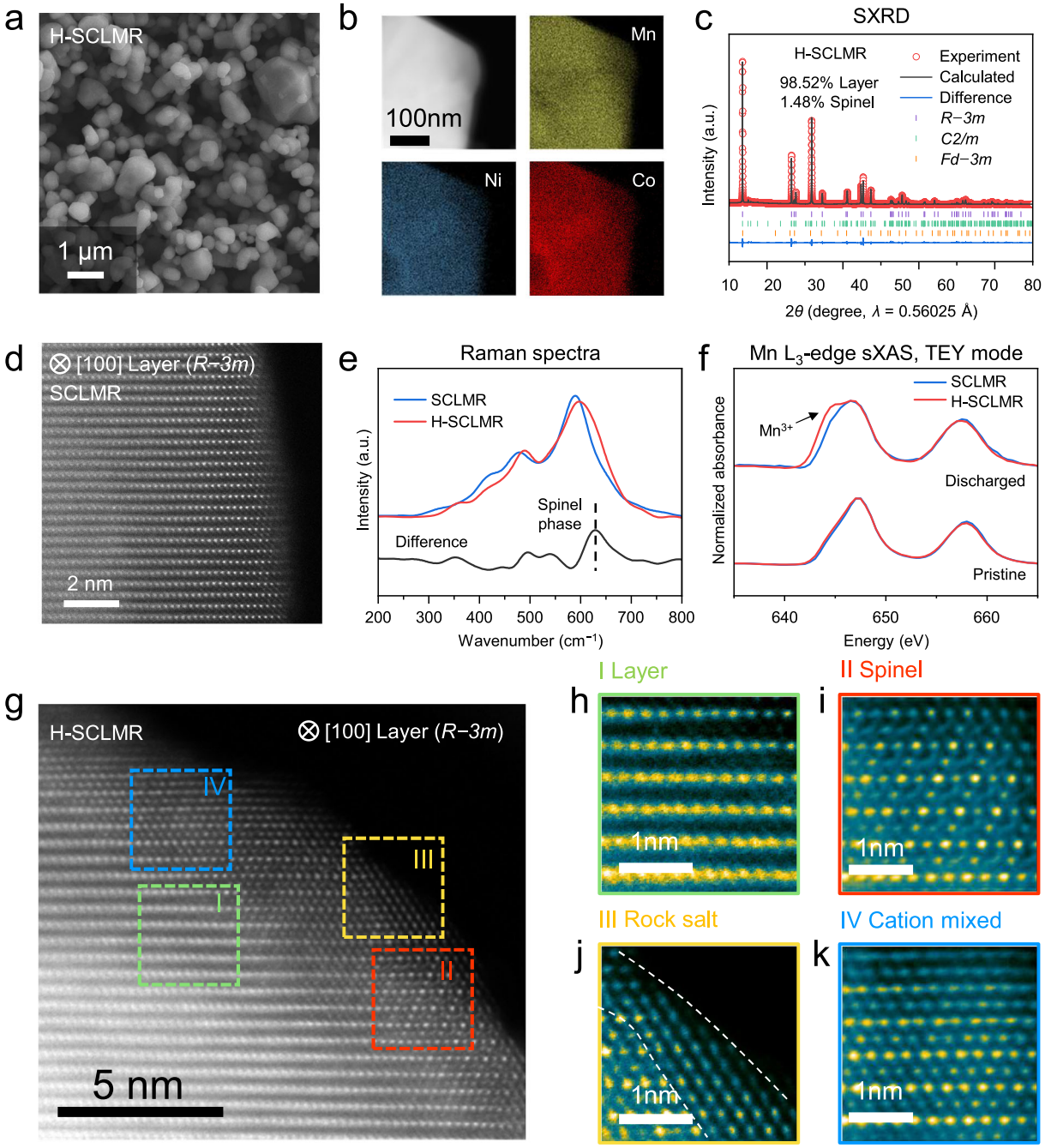

Fig. 1 | Structural characterizations of H-SCLMR. a SEM image of H-SCLMR. **b** EDS mapping of Mn, Ni, and Co in H-SCLMR. **c** SXRD and Rietveld refinement analysis of H-SCLMR. **d** Aberration-corrected HAADF STEM image of SCLMR at the near-surface region. **e** Comparation on Raman spectroscopy of H-SCLMR and SCLMR. **f** Mn L_3-edge sXAS of SCLMR and H-SCLMR at pristine and fully discharged states. **g** Aberration-corrected HAADF-STEM image taken near the surface and along the [100] direction of the layered ($R-3m$) phase. **h**–**k** Magnified region showing different cation ordering for **h** layered-, **i** spinel-type, **j** rock salt-, and **k** cation mixed-structures. Source data are provided as a Source Data file.

also consistent with H-SCLMR showing significantly higher discharge capacity below ~3.5 V (vs. Li^+/Li) than SCLMR and PCLMR at various rates, as shown in Fig. 2e. The origin of such anomalous trend of D_{Li} is discussed in Supplementary Note 2. The condition of potential-concentration linearity is demonstrate in Supplementary Note 3. The discharge curve of H-SCLMR shows a shoulder peak around 2.8 V (vs. Li^+/Li). In comparison, such a feature is absent for SCLMR and PCLMR. For better visualization, we presented the dQ/dV plot at 0.1 C/0.1 C charge/discharge in Fig. 2f. The redox peak at 2.8 V (vs. Li^+/Li) is clearly shown. In addition, the 2.8 V peak is manifested at a high rate of 5 C/5 C charge/discharge in Supplementary Fig. S11. We attributed this peak to lithiation of the surface phase, as indicated by the Mn L_3-edge sXAS results (Fig. 1f). This lithiation step is similar to the over-lithiation of $LiMn_2O_4$ spinel[44,45], yet our voltage is slightly higher, possibly due to the coexistence of multi-type cation ordering at the surface of H-SCLMR.

To investigate the end-of-discharge kinetics, we conducted a distribution of relaxation time (DRT) analysis based on the in situ electrochemical impedance spectra (EIS) collected during discharging. In comparison with SCLMR (Fig. 3a), H-SCLMR (Fig. 3c) shows significantly lower impedance at the end of discharge. The difference is more clearly revealed by DRT analysis. SCLMR shows significantly

https://doi.org/10.1038/s41467-026-75101-w

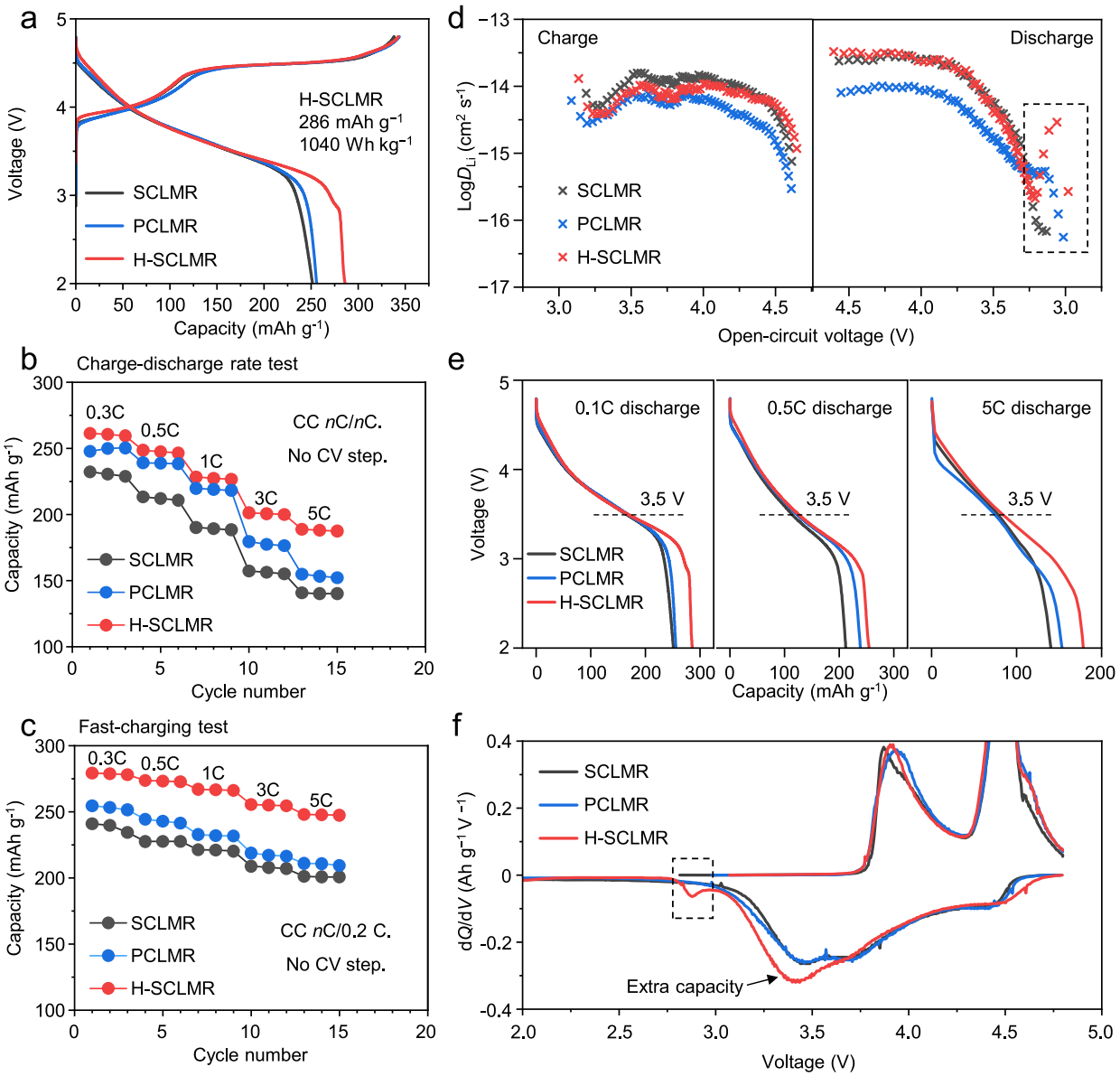

Fig. 2 | Electrochemical properties especially under high rates. a Charge-discharge curve of the formation cycle at 0.1 C (1 C defined as 250 mA g^{-1}) between 2.0 V and 4.8 V (vs. Li^+/Li). **b** Rate tests with the same charge and discharge rate. **c** Fast-charging tests with 0.2 C discharge and different charge rates. **d** D_{Li} calculated from GITT test. **e** Discharge curves of SCLMR, PCLMR and H-SCLMR at various rates. **f** *dQ/dV* plot at 0.1 C/0.1 C charge/discharge. All cells were tested under 30 °C Source data are provided as a Source Data file.

increased τ_2 peak height at ~ 1 s timescale (Fig. 3b), corresponding to the increased solid-state diffusion impedance within the electrodes[50]. In contrast, H-SCLMR shows no significant changes in high τ_2 peak height at the end-of-discharge period (Fig. 3d), indicating the maintenance of diffusion kinetics. White curves in Fig. 3b and d present the DRTs at the fully discharged state, where the more sluggish solid-state diffusion kinetics of SCLMR are clearly shown. These results confirm the fact that the diffusion kinetics at the end of the discharge limit the depth of discharge and discharge capacity, and the necessity of the surface spinel phase to enhance diffusion kinetics.

With the assistance of finite-element analysis (FEA) simulations, we found the relevance between the high-rate capability, the low-voltage electrochemical activity, the extra low-voltage capacity and the anomalous D_{Li} increase at the end-of-discharge period can be unified. Two models were constructed. The first represents H-SCLMR, consisting of a spherical LMR particle with a diameter of 1 µm coated by a 5 nm $LiMn_2O_4$ spinel layer. The second represents SCLMR and was designed as a control model, in which a 1 µm spherical LMR particle is coated with a 5 nm surface layer possessing identical properties to the bulk LMR.

Discharge processes were simulated for both models by applying an inward lithium flux at the particle surface. The simulated discharge curves are shown in Fig. 3e and exhibit good agreement with the experimentally measured discharge profiles. Although the surface spinel layer accounts for only ~1.5% of the total particle volume in the model, H-SCLMR exhibits a simulated capacity increase of 10.5%. This result can match the experimental capacity enhancement, and can imply that the improved capacity does not only originate from the additional capacity contribution of the surface phase itself, but also from enhanced overall reaction kinetics. Although the FEA simulations primarily represent idealized conditions, it provides assistance for understanding the enhancement of capacity and rate performance.

https://doi.org/10.1038/s41467-026-75101-w

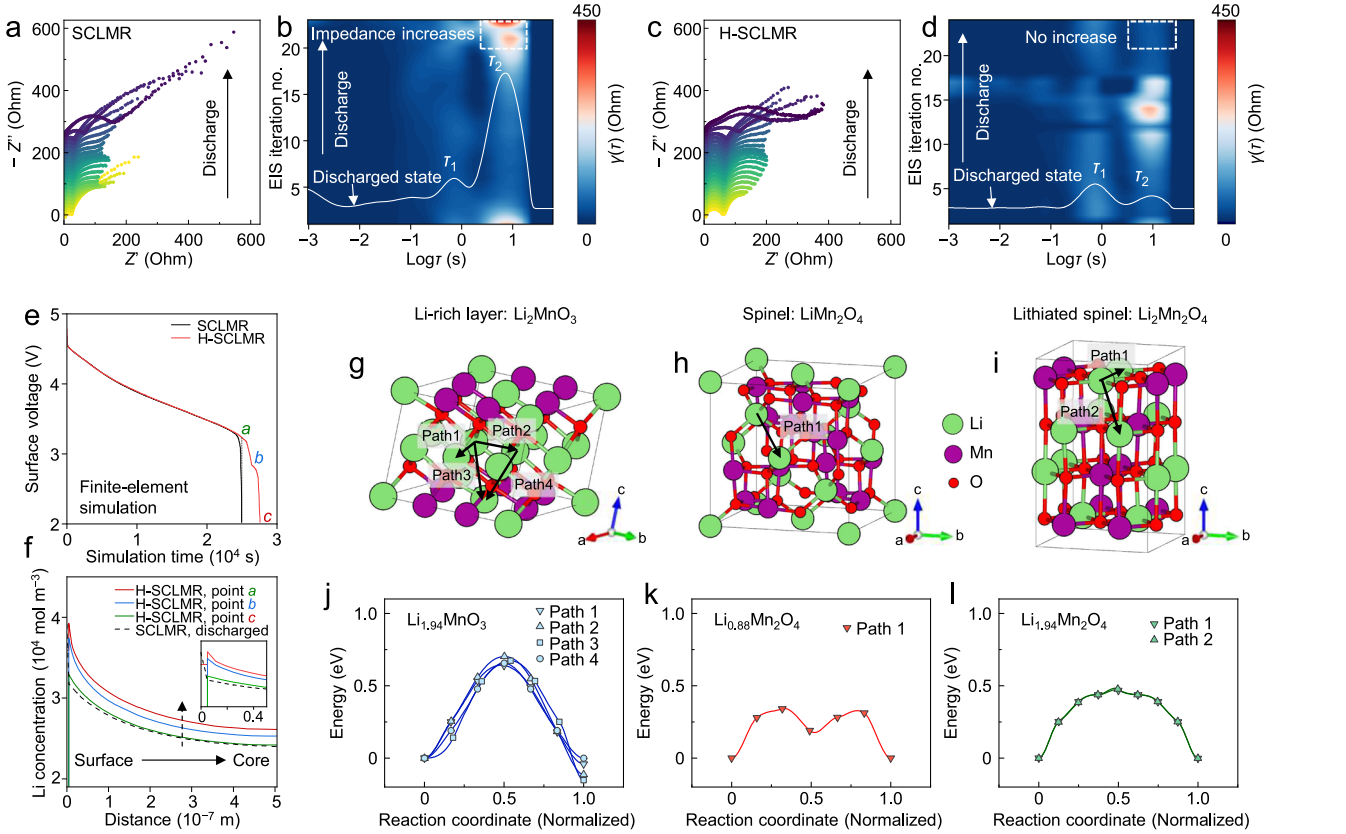

Fig. 3 | Diffusion kinetics analysis. a In situ EIS collected during discharging of SCLMR. Offsets are applied to improve the clarity. **b** DRT of SCLMR calculated from in situ EIS. White curve shows the DRT at discharged state. **c** In situ EIS collected during discharging of H-SCLMR. Offsets are applied to improve the clarity. **d** DRT of H-SCLMR calculated from in situ EIS. White curve shows the DRT at discharged state. The EIS tests were conducted at 30 °C. The cells were discharged at 0.1 (1 C defined as 250 mA g^{-1}) C from the fully charged states (4.8 V). **e** Simulated discharge voltage profiles of SCLMR and H-SCLMR. **f** Simulated radial Li concentration distributions at various states. Inset: enlarged view at the near-surface regime. Li^+ migration paths in Li_2MnO_3-type Li-rich layer structure (**g**), $LiMn_2O_4$-type spinel (**h**) and $Li_2Mn_2O_4$-type lithiated spinel (i). **j**–**l** Li^+ migration energy landscapes of $Li_{1.94}MnO_3$ (**j**), $Li_{0.88}Mn_2O_4$ (**k**) and $Li_{1.94}Mn_2O_4$ (**l**). Source data are provided as a Source Data file.

As shown in Supplementary Fig. S12a, when SCLMR reaches full discharge (corresponding to point *a* in Fig. 3e), an steep lithium concentration gradient develops near the surface. This can be also observed from the radial linescan of Li concentration (Fig. 3f). This arises because, at the end-of-discharge stage, the lithium diffusion coefficient of LMR decreases sharply with increasing lithium concentration. The accumulation of lithium near the surface further suppresses local D_{Li}, causing the surface potential of SCLMR to rapidly drop to 2.0 V, even though the particle core remains insufficiently lithiated. In contrast, when H-SCLMR reaches point *a*, although the lithium concentration distribution in the bulk is similar to that of SCLMR, the high lithium diffusivity of the $LiMn_2O_4$ surface layer prevents surface lithium accumulation and the associated rapid decrease in D_{Li}, allowing for further lithiation of bulk LMR (Supplementary Fig. S12b).

When H-SCLMR further discharges to point *b*, low-voltage over-lithiation of $LiMn_2O_4$ is activated, during which the surface potential remains nearly constant. This allows the bulk LMR to relax during surface lithiation, enabling lithium near the surface to diffuse inward toward the core under a nearly constant potential rather than continuing to accumulate at the surface. As a result, the lithiation depth of the bulk phase is further increased. Accordingly, Fig. 3f shows that while the lithium concentration near the core-shell interface at points *b* and *c* is similar, the lithium concentration in the bulk continues to increase. This behavior is further confirmed by the concentration-simulation time curves shown in Supplementary Fig. S12b. Once surface lithiation is activated, the increase in lithium concentration at the core-shell interface slows, while the lithium concentration at the particle center continues to rise. During surface over-lithiation, bulk lithiation proceeds simultaneously, explaining why the capacity observed at the low-voltage plateau exceeds the theoretical capacity contribution of the surface layer alone. Overall, an electrochemically active surface layer with high lithium-ion conductivity can serve as an effective "buffer", smoothing concentration gradients and promoting deeper lithiation of the bulk material. As a result, the particle core can withstand more sufficient lithiation (Supplementary Fig. S12a).

To validate that the kinetic enhancement originates from the surface spinel phases, we performed density functional theory (DFT) calculations with the climbing-image nudged elastic band (CI-NEB) method to investigate Li^+ diffusion behavior in supercells containing Li vacancies (see Methods for details). Figure 3l shows the energy landscapes for Li^+ migration along four paths in $Li_{1.94}MnO_3$ (Fig. 3g), representing diffusion in the Li-rich layered phase (Li_2MnO_3) during the end-of-discharge period. The migration barriers for paths 1-4 were 0.66, 0.76, 0.75 and 0.66 eV, respectively. For comparison, Fig. 3h and k present Li^+ migration in discharged $LiMn_2O_4$-type spinel ($Li_{0.88}Mn_2O_4$) showing a significantly lower barrier of 0.34 eV. Similarly, Fig. 3i and l display Li^+ migration in discharged $Li_2Mn_2O_4$-type lithiated spinel ($Li_{1.94}Mn_2O_4$) with barriers of 0.47 and 0.48 eV for two paths. As shown in Supplementary Fig. S13, the Li_2MnO_3 layered Li-rich phase exhibits substantially higher migration barriers (0.66–0.76 eV) compared to both spinel phases (0.34-0.48 eV), clearly demonstrating the better Li^+

https://doi.org/10.1038/s41467-026-75101-w

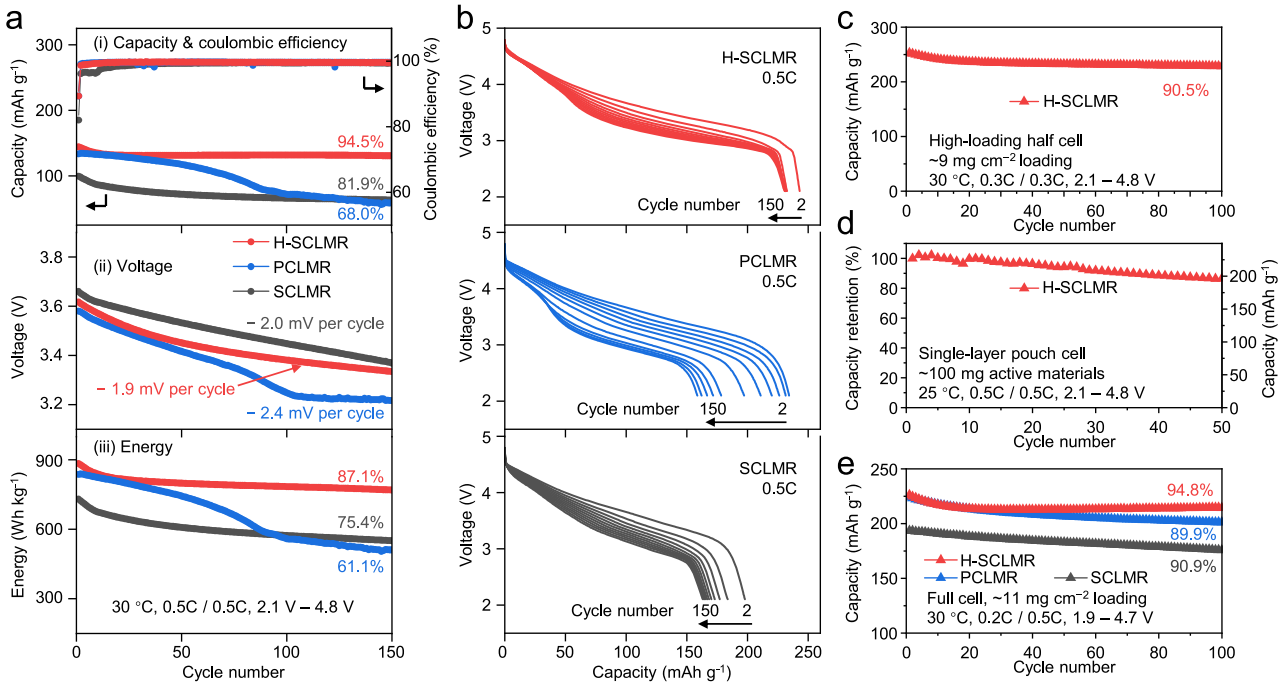

Fig. 4 | Cycling performance of H-SCLMR. a Comparison of the capacity retention (i), average discharge voltage retention (ii) and specific energy retention (iii) of H-SCLMR, SCLMR, and PCLMR at 0.5 C (1 C defined as 250 mA g^{-1}) between 2.1 and 4.8 V (vs. Li^+/Li) at 30 °C. **b** Discharge voltage profiles corresponding to (**a**). **c** Cycling performance of H-SCLMR in thick electrode condition with ~2.5 mAh cm^{-2} areal capacity at 0.3 C/0.3 C charge/discharge between 2.1 and 4.8 V (vs. Li^+/Li) at 30 °C. **d** Cycling performance of H-SCLMR in single-layer pouch-type cell containing ~100 mg active materials, at 0.5 C/0.5 C charge/discharge between 2.1-4.8 V (vs. Li^+/Li) at 25 °C. Inset: digital photo of the pouch cell. **e** Full-cell cycling tests based on graphite negative electrodes. Source data are provided as a Source Data file.

mobility in spinel structures that explains the observed kinetic improvements. Considering the above, our results demonstrate that a surface layer with high ionic conductivity and electrochemical activity can significantly enhance the kinetic performance of LMR materials, even when the layer is very thin. The rate capability of LMR is mostly limited by the surface and the surface-modified H-SCLMR can demonstrate enhanced diffusion kinetics and high-rate performance, especially suitable for fast-charging applications.

The cycling performance of H-SCLMR was evaluated under several conditions. Figure 4a compares the cycling of the three samples at 0.5 C between 2.1-4.8 V (vs. Li^+/Li) after two formation cycles at 0.1 C between 2.0-4.8 V (vs. Li^+/Li). After 150 cycles, H-SCLMR has 94.5% capacity retention (231 mAh g^{-1} discharge capacity), higher than 68.0% capacity retention for PCLMR and 81.9% for SCLMR (Fig. 4a(i)). The average voltage decay of H-SCLMR is 1.9 mV per cycle, lower than 2.0 mV per cycle for SCLMR, and 2.4 mV per cycle (Fig. 4a(ii)) for PCLMR. For discharge specific energy, H-SCLMR shows 87.1% retention (Fig. 4a(iii)) higher than 61.1% for PCLMR and 75.4% for SCLMR. The good cycling performances of H-SCLMR and SCLMR over PCLMR is in consistent with the previous understanding that single crystals have better mechanical properties and less surface side-reaction, while the lower capacity and specific energy of SCLMR than PCLMR is effectively resolved by the surface treatment. Figure 4b shows the evolution of the discharge voltage profiles during the cycling test presented in Fig. 4a. The most severe capacity and voltage fade was observed for PCLMR, while for SCLMR the shape of the voltage profile is better maintained. Though the widely observed voltage decay in LMRs still exists in H-SCLMR, it shows less voltage profile change than the other two samples, demonstrating the better stability of H-SCLMR than PCLMR and SCLMR upon cycling. Cycling performance of the samples was repeated twice for validation (Supplementary Fig. S14). We prepared thick electrode with 90 wt% active materials and ~9 mg cm^{-2} active material loading, corresponding to an areal capacity around 2.5 mAh cm^{-2}. Under these condition, H-SCLMR has 278 mAh g^{-1} discharge capacity at 0.3 C and 90.5% capacity retention after 100 cycles at 0.3 C/0.3 C charge/discharge between 2.1-4.8 V (vs. Li^+/Li) at 30 °C (Fig. 4c). For evaluations under harsher conditions, we tested at 0.8 C/0.8 C charge/discharge between 2.1 and 4.8 V (vs. Li^+/Li) at 50 °C (Supplementary Fig. S15), which also shows better high-temperature cycling stability of H-SCLMR than PCLMR and SCLMR. We prepared single-layer pouch-type cell containing ~100 mg active materials. Voltage profiles of the formation cycles are shown in Supplementary Fig. 16. At 0.5 C/0.5 C charge/discharge between 2.1 and 4.8 V (vs. Li^+/Li) at 25 °C, H-SCLMR has 86.6% capacity retention after 50 cycles (Fig. 4d). Lastly, all three samples were tested in full cell using a 11 mg cm^{-2} active materials loading. Graphite was used as the negative electrode, with N/P ratio controlled at around 1.2. Supplementary Fig. S17a, S17b and S17c shows the first two charge-discharge voltage profiles of the full cells based on H-SCLMR, SCLMR and PCLMR, respectively. Under such a high loading, H-SCLMR shows 94.8% capacity retention after 100 cycles (Fig. 4e) and the average CE of 2-100 cycles is as high as 99.89% (Supplementary Fig. S17d), which verifies the practical applicability of H-SCLMR. In comparison, the capacity retentions of PCLMR and SCLMR in full cells are 89.9% and 90.9% respectively.

For LMRs, one important factor influencing the cycling stability is the associated destructive lattice strain and anisotropic volume changes during cycling, particularly under deep lithiation and high local Li concentration gradients. One important factor contributing to the improved cycling stability of H-SCLMR and SCLMR over PCLMR is the mechanical stability of the grain-boundary-free single crystals. As shown by the cross-sectional SEM images of H-SCLMR and SCLMR electrodes before (Fig. 5a(i) and 5b(i)) and after cycling (Fig. 5a(ii) and 5b(ii)), the single crystals are crack-free. In comparison, PCLMR shows cracks and more cavities after cycling (Fig. 5c(i); after 150 cycles of the test in Fig. 5c(ii)). In the pristine SCLMR, the severe lithium

https://doi.org/10.1038/s41467-026-75101-w

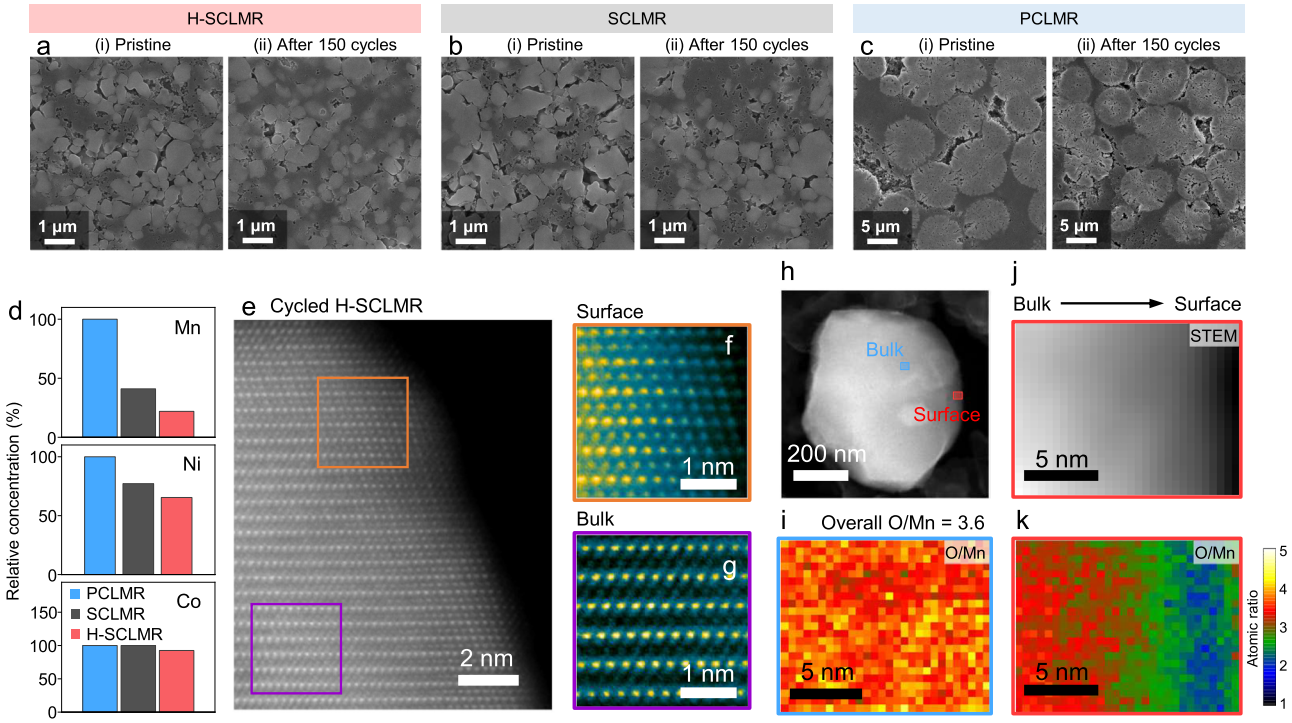

Fig. 5 | Suppressed degradations of H-SCLMR. a Cross-sectional SEM of H-SCLMR (i) before and (ii) after cycling. **b** Cross-sectional SEM of SCLMR (i) before and (ii) after cycling. **c** Cross-sectional SEM of PCLMR (i) before and (ii) after cycling. **d** Relative dissolved transition metal concentrations in transition metal dissolution tests. **e** Aberration-corrected HAADF STEM image of the surface region of the cycled H-SCLMR. **f** Magnified region of the surface in (**e**). **g** Magnified region of the bulk in (**e**). **h** STEM image of a cycled H-SCLMR particle. **i** EELS-resolved O/Mn ratio mapping in the bulk region of (**h**). **j** Magnified region of the surface in (**h**). **k** EELS-resolved O/Mn ratio mapping of (**j**). All the post-cycling data of the materials were collected at the discharged state after 150 cycles at 0.5 C (1 C defined as 250 mA g^{-1}) and 30 °C. Source data are provided as a Source Data file.

accumulation near the surface at the end-of-discharge stage leads to steep concentration gradients, which inevitably translate into highly localized chemo-mechanical stress at the particle surface and subsurface regions[38]. In contrast, the introduction of a thin, electrochemically active, and highly Li^+-conductive surface layer effectively homogenizes lithium transport across the particle-surface interface. As demonstrated by the finite-element simulations, the spinel shell mitigates lithium accumulation at the surface and promotes more uniform lithiation of the particle core. The effect of strain accumulation can be quantified by the lattice plane distance evolution. High-resolution SXRD analysis reveals that the lattice-plane spacing changes of the (003), (101), and (104) reflections after 150 cycles are limited to 0.019, 0.004, and 0.005 Å for H-SCLMR, respectively (Supplementary Fig. S18a). In comparison, the corresponding changes are 0.029, 0.010, and 0.010 Å for SCLMR (Supplementary Fig. S18b), and 0.020, 0.016, and 0.012 Å for PCLMR (Supplementary Fig. S18c). The minimal lattice distortion observed for H-SCLMR indicates high lattice stability, which we attribute to a more homogeneous stress distribution. These cracks and cavities substantially increase the interfacial contact area between electrochemically active positive electrode particles and the organic electrolyte, thereby accelerating coupled electrochemical, mechanical, and chemical degradation processes[51]. Therefore, the mechanical robustness offered by single-crystal morphology helps suppress side reactions such as transition metal dissolution. As shown by the ICP measurement of the transition metals dissolved in the organic electrolytes after cycling (Fig. 5d), H-SCLMR has 78% less Mn dissolution and 35% less Ni dissolution than PCLMR. The surface structure also matters, as supported by less Mn and Ni dissolution of surface-modified H-SCLMR than unmodified SCLMR.

Another key factor causing the degradation of LMRs is the oxygen-loss-related irreversible phase transformation. Differential electrochemical mass spectrometry (DEMS) measurements show that H-SCLMR delivers the lowest O_2 and CO_2 evolution (Supplementary Fig. S19). XPS measurements were conducted on all samples after the 1st and the 100th cycles. While all three materials show comparable surface Co stability during cycling (Supplementary Fig. S20a), noticeable differences are observed for Ni (Supplementary Fig. S20b) and Mn (Supplementary Fig. S20c). In particular, H-SCLMR exhibits the strongest resistance to surface Mn reduction, indicating surface structural stability against phase transformation. For Ni 2*p* XPS of PCLMR, the peak shift toward higher binding energies is accompanied by diminishment of the Ni^{2+} satellite signal, suggesting insufficient Ni reduction induced by degradation, which is consistent with its worst capacity retention. For better understanding of the stability of H-SCLMR, especially the effect of the surface phase, we conducted aberration-corrected STEM measurements of the cycled H-SCLMR. The bulk lattice has maintained the same layered structure (Supplementary Fig. S21a) as the pristine sample (Supplementary Fig. S9). Slight transition metal migration to the Li layer was observed, but no significant pores or phase changes occurred (Supplementary Fig. S21b). At the surface, we found a uniform 3 nm-thick cation-mixed-type structure (Fig. 5e) coherently bonded to the layered structure in the bulk (Fig. 5g). As magnified in Fig. 5f, the level of cation mixing is stronger than that in Fig. 1k but weaker than that in Fig. 1j. In contrast, the thickness of the reconstructed layer (primarily composed of rock salt and partially disordered phases) reaches ~8 nm, which is nearly three times that observed for cycled H-SCLMR (Supplementary Fig. S22). These indicate a surface densification process during cycling, but for H-SCLMR, the densification is constrained within only around 3 nm thick. Such constrained densified structure likely originates from the complex structure in the as-synthesized state, and the in situ formed densified layer could prevent further oxygen loss and structural changes. Given the intrinsically sluggish Li^+ transport kinetics of the rock-salt phase and its strong thickness dependence, the kinetic

penalty imposed by such a thin surface layer is substantially reduced compared to that of a much thicker reconstructed layer. The constrained thickness of the densified layer ensures the maintenance of capacity and rate performance, which explains the better cycling performance than SCLMR. Lastly, we evaluated the oxygen loss at the surface of H-SCLMR after cycling using electron energy loss spectroscopy (EELS, at local regions in Fig. 5h). To set a reference, Fig. 5i shows a uniform O/Mn ratio of 3.6 in the bulk lattice. At the surface, graded O/Mn ratio can be identified (Fig. 5j, k), with a value of ~2 at the surface and ~3.6 at <5 nm away from the surface. The lowered O/Mn ratio is attributed to surface oxygen loss and cation densification of the surface phase. It again indicates that the surface phase transformation during electrochemical cycling is limited to <5 nm region at the surface. This reinforces our results that the surface-modified single-crystal LMR benefits both high-rate performance and cycling stability.

Conclusions and outlook

To summarize, we reported progress in designing and producing high-rate single-crystal LMR with fast recharge capability. Our results demonstrate that Li-rich chemistry, single-crystal morphology, and rate capability can be simultaneously achieved via appropriate synthesis route. The challenge in realizing high-rate capacity of Li-rich layered oxides is largely due to the surface bottleneck, which can be effectively resolved by introducing Li^+-conductive and over-discharge-active surface phases with complex cation ordering within the same closely packed oxygen framework. Our findings deepen the understanding of electrochemically active surface phases to enhance overall kinetic properties. Looking forward, our approach can be combined with positive electrode coatings and electrolyte formulations to further improve the cycling stability and suppress voltage decay of LMR. As the intrinsic high-rate capability of single-crystal Li-rich layered oxides has now been demonstrated, our work beckons further explorations of coarse-grain and Li-excess positive electrode materials which were conventionally thought to be inappropriate for fast-charging applications.

Methods

Material synthesis

All LMR materials used in this work were synthesized from a $Mn_{0.6}Ni_{0.2}Co_{0.2}CO_3$ precursor. $Mn_{0.6}Ni_{0.2}Co_{0.2}CO_3$ precursors were prepared by a co-precipitation method. $MnSO_4{\cdot}5H_2O$ (analytical purity, Sigma Aldrich), $NiSO_4{\cdot}6H_2O$ (analytical purity, Sigma Aldrich), and $CoSO_4{\cdot}7H_2O$ (analytical purity, Sigma Aldrich) with 3:1:1 molar ratio were dissolved in deionized water to form a homogeneous solution with a total transition metal molar concentration (Mn+Ni+Co) of 1.0 M. Co-precipitation was performed using 1.0 M Na_2CO_3 (analytical purity, Sigma Aldrich) under a reaction temperature of 60 °C. After aging for 12 h, the precipitates were collected and washed by deionized water and dried at 110 °C under vacuum to obtain $Mn_{0.6}Ni_{0.2}Co_{0.2}CO_3$ precursors.

SCLMR was prepared by a eutectic salts-assisted method reported in our previous work[20]. In brief, the $Mn_{0.6}Ni_{0.2}Co_{0.2}CO_3$ precursors were firstly calcined at 600 °C for 5 h to obtain the spinel-type M_3O_4 precursors. M_3O_4 precursors were mixed with a eutectic lithium-salt mixture consisting of $LiOH{\cdot}H_2O$ (analytical purity, Sigma Aldrich) and $LiNO_3$ (analytical purity, Sigma Aldrich) at a molar ratio of 0.95:0.53:1 ($LiOH:LiNO_3$:*M*) and deagglomerated using a planetary centrifugal mixer (AR-100, THINKY) at 2000 rpm (around 465 g force) for 12 min. The obtained mixture was then calcinated at 960 °C for 2 h and then at 800 °C for 10 h in air to obtain SCLMR. The under-stoichiometry and over-stoichiometry samples were synthesized using the same procedure as SCLMR, with Li/*M* ratio adjusted between 1.35 and 1.55 accordingly. H-SCLMR was prepared by further treatment of SCLMR. SCLMR powders were dispersed in aqueous solution of $(NH_4)_2SO_4$ (analytical purity, Sigma Aldrich). The solution was then dried at 90 °C. The amount of $(NH_4)_2SO_4$ was optimized to be 5 wt% of SCLMR (Supplementary Fig. S6). The dried powders were calcined at 300°C for 10 h followed by cooling down to around 25 °C. The calcined powders were washed by deionized water and annealed at 300 °C for 5 h to obtain H-SCLMR. PCLMR was prepared by a conventional solid-state reaction method. $Mn_{0.6}Ni_{0.2}Co_{0.2}CO_3$ precursors were hand-mixed with Li_2CO_3 (analytical purity, Sigma Aldrich) at Li:*M* = 1.40 with pestle and mortar. The mixture was then calcined at 900°C for 10 h to obtain PCLMR. All heating and cooling rates in this work were set to be 5 °C min^{-1}.

Electrochemical measurements

Electrochemical properties were tested in CR2032-type with 20 mm diameter. The case and the spring used for coin cell were made with stainless steel. Each coin cell contains one positive electrode and one negative electrode. Positive electrode slurries were prepared by mixing the positive electrode active materials, super P carbon (Timcal), carbon nanotube (XFM13, Nanjing XFNANO Materials Tech Co., Ltd) and polyvinylidene fluoride (Solef 5130, molecular weight 1,000,000–1,200,000 Da, Solvay) with a weight ratio of 80:8:2:10 using N-methyl-1,2-pyrrolidone (analytical purity, Sigma Aldrich) as the solvent. The obtained slurries were coated on 16 μm thick Al foils (99.5%) using an automatic coating machine (MSK-AFA-SC200, MTI), followed by drying under vacuum at 110 °C and punching into disks with 12 mm diameter using a cutting machine (MSK-T10, MTI). For thick electrodes, the weight ratio of positive electrode active materials, super P carbon, carbon nanotube and polyvinylidene fluoride was adjusted to be 90:4:1:5. Positive electrode active materials loading was controlled to be around 5.0 mg cm^{-2} for pouch cell fabrication, around 9.0 mg cm^{-2} for thick electrodes, 11 mg cm^{-2} for full cell tests and 2.5–3.0 mg cm^{-2} in other tests. Graphite electrode was prepared by mixing the active materials, super P carbon and polyvinylidene fluoride dissolved in N-methyl-1,2-pyrrolidone with a mass ratio of 8:1:1, then coated onto 12 μm thick Cu foils (99.5%) with a negative to positive (N/P) ratio of around 1.2. Coin cells were assembled in an Ar-filled glovebox using lithium metal (400 μm thick and 15 mm diameter, 99% purity, provided by Ganfeng Lithium Group Co., Ltd) as the negative electrode and one Celgard-2325 membrane (19 mm diameter) as the separator. Celgard-2325 is a 25 μm thick trilayer polypropylene/polyethylene/polypropylene lithium-ion battery separator with a porosity of approximately 39%, and an average pore size of about 0.027 μm. In this work, Li metal was used as received, stored in an Ar-filled glove box, and used within four weeks after being obtained. Electrolytes used in all tests were 1 M $LiPF_6$ dissolved in ethylene carbonate: dimethyl carbonate: diethyl carbonate = 1:1:1 (vol%) solvent with 1 wt% $LiPO_2F_2$ as an additive (99.5%, electrolyte vendor: DoDoChem Inc.). Electrolytes were used without further purification. The amount of the electrolytes used for each coin cell is 100 μL. Single-layer pouch cells were assembled in Ar-filled glove box using a 40 × 50 mm positive electrode and lithium metal negative electrode (200 μm thick and 45 × 55 mm diameter, 99% purity, provided by Ganfeng Lithium Group Co., Ltd). 60 × 70 mm aluminum laminate pouches were used. The amount of electrolytes injected into the pouch cell was 6 μL per mg positive electrode active materials. After the cell stack is placed inside the aluminum laminate pouch, the open sides are heat-sealed under reduced pressure to eliminate residual gases and ensure tight contact between the layers.

All coin cells were tested under 30 °C (except for high-temperature cycling tests) using a constant-temperature NEWARE battery test system. After assembling, the cells were rested for at least 8 h, and then cycled at conditions specified in the manuscript. Rate tests were conducted using CC *n*C/*n*C charge-discharge cycles with *n* ranges from 0.3 C to 5 C. Fast-charging tests were conducted using CC *n*C/0.2 C charge-discharge cycles with *n* ranges from 0.3 C to 5 C. No constant voltage (CV) step was used in the rate tests. GITT tests were conducted by charge/discharge at 0.1 C pulse current for 10 min and

relax for 90 min, with data points collected every 10 s. For in situ EIS, cells were discharged from 4.8 V to 2.0 V (0.2 C, 15 min discharge + 30 min rest), followed by EIS (10 mHz-7 MHz). A potentiostatic signal (±10 mV) was applied with 20 data points per decade of frequency, and the measurements were carried out under operating conditions that included a 30 min open-circuit voltage (OCV) equilibration period prior to the test.

DRT data were obtained and analyzed using pyDRTtools[52,53]. Galvanostatic cycling tests were conducted with a voltage range of 2.1–4.8 V (vs. Li^+/Li) and a charge/discharge rate of 0.5 C/0.5 C. Cycling tests of high-loading positive electrode were conducted at 0.3 C/0.3 C to mitigate the degradation of the lithium metal negative electrode. High-temperature cycling tests were conducted at 50 °C. Pouch cells were tested using a LAND battery test system at 25 °C. Pouch cells were rested for 24 h, cycled at 2.0-4.8 V (vs. Li^+/Li) and 0.1 C for two formation cycles, and then cycled at 0.5 C and 2.1–4.8 V (vs. Li^+/Li). The full cells were assembled in an argon-filled glovebox using Celgard-2320 membrane (100 mm width) as the separator. Celgard-2320 is a 20 μm thick trilayer polypropylene/polyethylene/polypropylene lithium-ion battery separator with a porosity of approximately 39%, and an average pore size of about 0.027 μm. The electrolyte was 1 M $LiPF_6$ dissolved in ethylene carbonate: dimethyl carbonate: diethyl carbonate = 1:1:1 (vol%) solvent with 1 wt% $LiPO_2F_2$ as an additive. The full cell was rested for ≥8 h and cycled at 1.8–4.75 V (0.1 C) twice for formation, and then cycled at 0.2 C charge/0.5 C discharge at 1.9-4.7 V.

Structural characterizations

Before conducing characterizations on the powder samples, the samples were prepared directly in air under 25 °C. Powder XRD was conducted on a Brucker D8 Advance X-ray diffractometer in the 2θ range of 10°–80° with 1°/min scan rate using Cu Kα radiation (λ = 1.5418 Å). Rietveld refinements were conducted using FullProf software[54]. High-resolution SXRD measurements were conducted at TPS 19A1 beamline (λ = 0.56025 Å). SEM was conducted on a Zeiss Merlin Field Emission SEM. TEM and EDS were conducted on a JEM 2100Plus TEM. XPS was conducted on a Thermo Scientific K-Alpha+ X-ray photoelectron spectrometer using monochromic Al Kα radiation. The XPS binding energy scale was calibrated using the C 1*s* peak of adventitious carbon at 284.8 eV as a reference. All recorded spectra were normalized by subtracting a Shirley-type background, and the peak positions were adjusted accordingly to correct for any charging effects. Raman was conducted on a RENISHAW inVia confocal Raman microscope with a 532 nm laser. Elementary compositions were characterized by ICP-OES (Perkin Elmer). Surface area was measured by the Brunauer-Emmett-Teller (BET) method. The electrode samples, either before or after cycling, were prepared in an Ar-filled glovebox at 25 °C and were transferred for further characterizations after being vacuum-sealed in polypropylene bags. Electrode samples for cross-sectional SEM imaging were prepared by cutting and polishing the electrodes using a Leica EM TIC 3X Ion Beam Milling System. The post-cycling electrode samples were obtained by disassembling the coin cells in a glovebox and rinsed three times with diethyl carbonate (analytical purity, Sigma Aldrich), and dried in an Ar-filled glovebox before characterizations. For the transition metal dissolution tests, the electrodes were immersed in the same electrolyte as the electrochemical tests after charged to 4.8 V (vs. Li^+/Li) and placed for 2 weeks at 30 °C. Dissolved transition metal concentration in the electrolytes were then measured by ICP-mass spectrometer (ICP-MS, Perkin Elmer). For SXRD experiments, the material was scraped off the aluminum foil and placed into a 0.3 mm diameter glass capillary tube for measurement. For STEM experiments without ion milling, the material was scraped off the aluminum foil and loaded onto an 80-mesh copper grid for sample preparation. For other characterizations, the electrode sheets were used directly without further treatment. Mn L_3-edge sXAS measurements were conducted at beamline 4B7B of Beijing Synchrotron Radiation Facility. The spectrum was normalized by subtracting a linear background fitted through the data points at 535 and 565 eV, followed by scaling to the post-edge intensity.

Thin samples, including pristine and cycled H-SCLMR for STEM characterizations were prepared using a focus ion beam (FIB)-SEM system (Crossbeam 340, Zeiss) following standard lift-out procedure[55]. After lift-out, the samples were thinned and polished by a Ga ion beam to around 80 nm until electron transparency at 5 kV SEM. Other samples for STEM characterizations were prepared by directly dispersed the powder onto Cu meshes coated with ultrathin carbon film. STEM-HAADF imaging was conducted on aberration-corrected FEI-Titan Cubed Themis G2 300 STEM operating at 300 kV. EELS measurements were conducted on the same microscope. STEM and EELS data were analyzed using Digital Micrograph (ver. 3.61) and ImageJ software[56].

Simulations

The finite-element simulations were conducted using COMSOL Multiphysics. D_{Li} of LMR was derived from the GITT test of SCLMR. D_{Li} of $LiMn_2O_4$ was set to be 3.5×10^{-9} cm^2 s^{-1}, which was based on the average D_{Li} value reported for $LiMn_2O_4$ at different states in ref. 57

The DFT calculations in this study were performed using Vienna Ab initio Simulation Package (VASP) within the projector augmented-wave approach[58]. Perdew–Burke–Ernzerhof (PBE)[59] generalized-gradient approximation (GGA) functionals were adopted in all calculations. The DFT + U method was used to model electrons on the transition metal centers[60,61]. The on-site Hubbard term (U) was set to be 3.9 eV for Mn, which were suggested by Materials Project[62,63]. All calculations were spin-polarized, using a plane-wave cutoff of 520 eV and a Gamma k-point mesh with a spacing of <0.05 Å.

The original structure of Li_2MnO_3, $LiMn_2O_4$ and $Li_2Mn_2O_4$ were obtained from Materials Project[62]. Geometry optimizations of the unit cells were considered converged when the force on each atom was <0.01 eV $Å^{-1}$. Supercells containing 2 × 1 × 2 (96 atoms) and 2 × 2 × 1 (128 atoms) unit cells were constructed for Li_2MnO_3 and $Li_2Mn_2O_4$ respectively. Unit cell of $LiMn_2O_4$ containing 56 atoms were used directly. Supercells with single Li vacancy were constructed by removing one specific Li (depending on the vacancy site) atom from each supercell, the formula of the obtained supercells are $Li_{1.94}MnO_3$, $Li_{0.88}Mn_2O_4$ and $Li_{1.94}Mn_2O_4$ for Li_2MnO_3, $LiMn_2O_4$ and $Li_2Mn_2O_4$ respectively. The supercells were relaxed until the force on each atom was <0.01 eV $Å^{-1}$.

The climbing-image nudged elastic band (CINEB) calculations were performed to calculate the migration pathway and correspondent energy landscape[64,65]. The CINEB calculations were stopped once the force on each image was smaller than 0.02 eV/Å. The energies of the initial state and the final state may be different. Thus, the kinetically resolved activation barriers ΔE_{KRA} are reported throughout:

$$\Delta E_{KRA} = E_{TS} - (E_i + E_f) \quad (1)$$

where E_i and E_f are the energies of the initial and final states, and E_{TS} is the energy of the transition state[66]. The initial and final configurations in CINEB calculations are included in Supplementary Data 1-3.

Data availability

Data generated and analyzed in the present work are available in the manuscript or supplementary information. Source data are provided with this paper.

References

1. Liu, Y., Zhu, Y. & Cui, Y. Challenges and opportunities towards fast-charging battery materials. *Nat. Energy* **4**, 540–550 (2019).
2. Ahmed, S. et al. Enabling fast charging–a battery technology gap assessment. *J. Power Sources* **367**, 250–262 (2017).
3. Tarascon, J. M. & Armand, M. Issues and challenges facing rechargeable lithium batteries. *Nature* **414**, 359–367 (2001).

4. Goodenough, J. B. & Park, K.-S. The Li-ion rechargeable battery: a perspective. *J. Am. Chem. Soc.* **135**, 1167–1176 (2013).
5. Zhang, M. et al. Pushing the limit of 3*d* transition metal-based layered oxides that use both cation and anion redox for energy storage. *Nat. Rev. Mater.* **7**, 522–540 (2022).
6. Choi, J. W. & Aurbach, D. Promise and reality of post-lithium-ion batteries with high energy densities. *Nat. Rev. Mater.* **1**, 16013 (2016).
7. Zheng, M., Zhu, X., Zheng, H., Bo, Z. & Lu, J. Deployment strategies for Li-rich cathode materials in batteries. *Nat. Energy* **10**, 789–792 (2025).
8. Yu, X. et al. Understanding the rate capability of high-energy-density Li-rich layered $Li_{1.2}Ni_{0.15}Co_{0.1}Mn_{0.55}O_2$ cathode materials. *Adv. Energy Mater.* **4**, 1300950 (2014).
9. He, W. et al. Challenges and recent advances in high capacity Li-rich cathode materials for high energy density lithium-ion batteries. *Adv. Mater.* **33**, 2005937 (2021).
10. Liu, T. et al. Understanding Co roles towards developing Co-free Ni-rich cathodes for rechargeable batteries. *Nat. Energy* **6**, 277–286 (2021).
11. Li, M. & Lu, J. Cobalt in lithium-ion batteries. *Science* **367**, 979–980 (2020).
12. Li, B. et al. Decoupling the roles of Ni and Co in anionic redox activity of Li-rich NMC cathodes. *Nat. Mater.* **22**, 1370–1379 (2023).
13. Dong, Y. & Li, J. Oxide cathodes: functions, instabilities, self healing, and degradation mitigations. *Chem. Rev.* **123**, 811–833 (2023).
14. Zheng, H. et al. Optimizing oxygen redox activity by local chemical disorder toward robust Co-Free Li-rich cathode with high voltage stability. *Adv. Mater.* **37**, 2414443 (2025).
15. Liu, T. et al. Origin of structural degradation in Li-rich layered oxide cathode. *Nature* **606**, 305–312 (2022).
16. Zhang, Y. et al. Revealing Li-ion diffusion kinetic limitations in micron-sized Li-rich layered oxides. *Energy Storage Mater.* **53**, 763–773 (2022).
17. Langdon, J. & Manthiram, A. A perspective on single-crystal layered oxide cathodes for lithium-ion batteries. *Energy Storage Mater.* **37**, 143–160 (2021).
18. Li, B. et al. Perspectives on the practicability of Li-Rich NMC layered oxide cathodes. *Adv. Mater.* **36**, 2400259 (2024).
19. Liu, X. et al. Origin and regulation of oxygen redox instability in high-voltage battery cathodes. *Nat. Energy* **7**, 808–817 (2022).
20. Yoon, M. et al. Eutectic salt-assisted planetary centrifugal deagglomeration for single-crystalline cathode synthesis. *Nat. Energy* **8**, 482–491 (2023).
21. Yang, H., Wang, C.-A. & Dong, Y. Energy ceramic design for robust battery cathodes and solid electrolytes. *Adv. Powder Mater.* **3**, 100185 (2024).
22. Bi, Y. et al. Reversible planar gliding and microcracking in a single-crystalline Ni-rich cathode. *Science* **370**, 1313–1317 (2020).
23. van Bommel, A. & Dahn, J. R. Synthesis of spherical and dense particles of the pure hydroxide phase $Ni_{1/3}Mn_{1/3}Co_{1/3}(OH)_2$. *J. Electrochem. Soc.* **156**, A362 (2009).
24. You, B. et al. Research progress of single-crystal nickel-rich cathode materials for lithium ion batteries. *Small Methods* **5**, 2100234 (2021).
25. Zhu, X. et al. Tailoring redox couples of Li-rich Mn-based cathode materials by in-situ surface reconstruction for high-performance lithium-ion batteries. *Nano Energy* **134**, 110588 (2025).
26. Huang, H. et al. Pulse high temperature sintering to prepare single-crystal high nickel oxide cathodes with enhanced electrochemical performance. *Adv. Energy Mater.* **13**, 2203188 (2023).
27. Li, H. et al. Synthesis of single crystal $LiNi_{0.88}Co_{0.09}Al_{0.03}O_2$ with a two-step lithiation method. *J. Electrochem. Soc.* **166**, A1956 (2019).
28. Mesnier, A. & Manthiram, A. Influence of single-crystalline morphology on the electrochemical behavior of high-nickel layered oxide cathodes. *J. Electrochem. Soc.* **170**, 080509 (2023).
29. Zhang, B. et al. Does single-crystallization a feasible direction for designing Li-rich layered cathodes? *Energy Storage Mater.* **62**, 102926 (2023).
30. Zhao, X. et al. Perspective on high-stability single-crystal Li-rich cathode materials for Li-ion batteries. *ACS Appl. Mater. Inter.* **16**, 24147–24161 (2024).
31. Yang, Y. et al. Unlocking the potential of Li-rich Mn-based oxides for high-rate rechargeable lithium-ion batteries. *Adv. Mater.* **35**, 2307138 (2023).
32. Luo, D. et al. A Li-rich layered oxide cathode with negligible voltage decay. *Nat. Energy* **8**, 1078–1087 (2023).
33. Sun, J. et al. Restraining oxygen release and suppressing structure distortion in single-crystal Li-rich layered cathode materials. *Adv. Funct. Mater.* **32**, 2110295 (2022).
34. Wu, T. et al. Gradient "single-crystal" Li-rich cathode materials for high-stable lithium-ion batteries. *Adv. Funct. Mater.* **33**, 2210154 (2023).
35. Gu, K., Shi, Z., Li, X., Qiu, B. & Liu, Z. Review on the synthesis of Li-rich layered oxide cathodes. *J. Mater. Chem. A* **12**, 24727–24745 (2024).
36. Yu, D. Y. W., Yanagida, K. & Nakamura, H. Surface modification of Li-excess Mn-based cathode materials. *J. Electrochem. Soc.* **157**, A1177–A1182 (2010).
37. Hao, Z. et al. Suppressing Bulk strain and surface O_2 release in Li-rich cathodes by just tuning the Li content. *Adv. Mater.* **36**, 2307617 (2024).
38. Csernica, P. M. et al. Substantial oxygen loss and chemical expansion in lithium-rich layered oxides at moderate delithiation. *Nat. Mater.* **24**, 92–100 (2025).
39. McColl, K., Coles, S. W., Zarabadi-Poor, P., Morgan, B. J. & Islam, M. S. Phase segregation and nanoconfined fluid O_2 in a lithium-rich oxide cathode. *Nat. Mater.* **23**, 826–833 (2024).
40. Marie, J.-J. et al. Trapped O_2 and the origin of voltage fade in layered Li-rich cathodes. *Nat. Mater.* **23**, 818–825 (2024).
41. Zhu, Z. et al. Gradient Li-rich oxide cathode particles immunized against oxygen release by a molten salt treatment. *Na. Energy* **4**, 1049–1058 (2019).
42. Xu, B., Fell, C. R., Chi, M. & Meng, Y. S. Identifying surface structural changes in layered Li-excess nickel manganese oxides in high voltage lithium ion batteries: A joint experimental and theoretical study. *Energy Environ. Sci.* **4**, 2223–2233 (2011).
43. Liu, T. et al. Ultrastable cathodes enabled by compositional and structural dual-gradient design. *Nat. Energy* (2024).
44. Ji, H. et al. Ultrahigh power and energy density in partially ordered lithium-ion cathode materials. *Nat. Energy* **5**, 213–221 (2020).
45. Huang, Y. et al. Lithium Manganese Spinel Cathodes for Lithium-Ion Batteries. *Adv. Energy Mater.* **11**, 2000997 (2021).
46. Lee, J. et al. Unlocking the potential of cation-disordered oxides for rechargeable lithium batteries. *Science* **343**, 519–522 (2014).
47. Huang, Y. et al. Integrated rocksalt–polyanion cathodes with excess lithium and stabilized cycling. *Nat. Energy* (2024).
48. Baddour-Hadjean, R. & Pereira-Ramos, J.-P. Raman microspectrometry applied to the study of electrode materials for lithium batteries. *Chem. Rev.* **110**, 1278–1319 (2010).
49. Cai, Z. et al. In situ formed partially disordered phases as earth-abundant Mn-rich cathode materials. *Nat. Energy* **9**, 27–36 (2024).
50. Lu, Y., Zhao, C.-Z., Huang, J.-Q. & Zhang, Q. The timescale identification decoupling complicated kinetic processes in lithium batteries. *Joule* **6**, 1172–1198 (2022).
51. Xue, W. et al. Ultra-high-voltage Ni-rich layered cathodes in practical Li metal batteries enabled by a sulfonamide-based electrolyte. *Nat. Energy* **6**, 495–505 (2021).
52. Wan, T. H., Saccoccio, M., Chen, C. & Ciucci, F. Influence of the discretization methods on the distribution of relaxation times

deconvolution: implementing radial basis functions with DRTtools. *Electrochimi. Acta* **184**, 483–499 (2015).
53. Maradesa, A., Py, B., Wan, T. H., Effat, M. B. & Ciucci, F. Selecting the regularization parameter in the distribution of relaxation times. *J. Electrochem. Soc.* **170**, 030502 (2023).
54. Rodriguezcarvajal, J. Recent advances in magnetic-structure determination by neutron powder diffraction. *Phys. B* **192**, 55–69 (1993).
55. Yan, P. et al. Injection of oxygen vacancies in the bulk lattice of layered cathodes. *Nat. Nanotech* **14**, 602–608 (2019).
56. Schneider, C. A., Rasband, W. S. & Eliceiri, K. W. NIH Image to ImageJ: 25 years of image analysis. *Nat. Methods* **9**, 671–675 (2012).
57. Ouyang, C., Shi, S., Wang, Z., Huang, X. & Chen, L. Experimental and theoretical studies on dynamic properties of Li ions in $Li_xMn_2O_4$. *Solid State Commun.* **130**, 501–506 (2004).
58. Kresse, G. & Furthmuller, J. Efficiency of ab-initio total energy calculations for metals and semiconductors using a plane-wave basis set. *Comput. Mater. Sci.* **6**, 15–50 (1996).
59. Perdew, J. P., Ernzerhof, M. & Burke, K. Rationale for mixing exact exchange with density functional approximations. *J. Chem. Phys.* **105**, 9982–9985 (1996).
60. Vosko, S. H., Wilk, L. & Nusair, M. Accurate spin-dependent electron liquid correlation energies for local spin-density calculations - a critical analysis. *Can. J. Phys.* **58**, 1200–1211 (1980).
61. Jain, A. et al. Formation enthalpies by mixing GGA and GGA plus *U* calculations. *Phys. Rev. B* **84**, 10 (2011).
62. Jain, A. et al. Commentary: The Materials Project: a materials genome approach to accelerating materials innovation. *APL Mater.* **1**, 11 (2013).
63. Jain, A. et al. A high-throughput infrastructure for density functional theory calculations. *Comput. Mater. Sci.* **50**, 2295–2310 (2011).
64. Henkelman, G., Uberuaga, B. P. & Jónsson, H. A climbing image nudged elastic band method for finding saddle points and minimum energy paths. *J. Chem. Phys.* **113**, 9901–9904 (2000).
65. Henkelman, G. & Jónsson, H. Improved tangent estimate in the nudged elastic band method for finding minimum energy paths and saddle points. *J. Chem. Phys.* **113**, 9978–9985 (2000).
66. Van der Ven, A., Ceder, G., Asta, M. & Tepesch, P. D. First-principles theory of ionic diffusion with nondilute carriers. *Phys. Rev. B* **64**, 17 (2001).

Acknowledgements

This work was carried out with the support of 4B7B beamline at Beijing Synchrotron Radiation Facility under proposal nos. G4B7B-251018-001. The high-resolution SXRD experiments were carried out with the support of TPS 19A1 beamline under proposal nos. 2025-2-059-1.

Author contributions

J. Zhang, C.-A. Wang, J. Li, and Y. Dong conceived the project. J. Zhang and Y. Dong designed the experiments and analyzed the data. J. Zhang, S. Chen, Y. Xia, R. Tong, Y. Xiao, and Z. Liu synthesized the materials and conducted the electrochemical testing. J. Zhang, Y. Xia, Y. Xiao, and M. Fan conducted the structural characterizations. Z. Lv contributed to TEM. Y. Liao contributed to pouch cell assembly. M. Zhou contributed to finite-element simulations. M. Yoon contributed to the data analysis. J. Zhang, C.-A. Wang, J. Li, and Y. Dong wrote the manuscript. All authors discussed and contributed to the writing.

Funding

Y.H. Dong discloses support for the research of this work from the National Natural Science Foundation of China (grant number 52472074). C.-A.Wang discloses support for publication of this work from the National Natural Science Foundation of China (grant number 52173257 and 52372064).

Competing interests

The authors declare no competing interests.

Additional information

Supplementary information The online version contains supplementary material available at https://doi.org/10.1038/s41467-026-75101-w.

Correspondence and requests for materials should be addressed to Yanhao Dong, Ju Li or Chang-An Wang.

Peer review information *Nature Communications* thanks Jun Chen and the other anonymous reviewer(s) for their contribution to the peer review of this work. A peer review file is available.

Supplementary information

High-rate single-crystalline Li-rich layered oxide with diversified surface-phase cation ordering for Li-ion batteries

Jingxi Zhang[1], Shile Chen[1], Yuting Xia[1], Ye Xiao[1], Meicen Fan[1], Rong-Ao Tong[1], Zehui Liu[1], Zhuoran Lv[2], Yaqi Liao[3], Moonsu Yoon[4], Mengyuan Zhou[3], Yanhao Dong[1,*] , Ju Li[5,6,*], Chang-An Wang[1,*]

[1]*State Key Laboratory of New Ceramic Materials, School of Materials Science and Engineering, Tsinghua University, Beijing 100084, China*

[2]*State Key Lab of Metal Matrix Composites, School of Materials Science and Engineering, Shanghai Jiao Tong University, Shanghai 200240, China*

[3]*State Key Laboratory of Material Processing and Die and Mold Technology, School of Materials Science and Engineering, Huazhong University of Science and Technology, Wuhan 430074, China*

[4]*Department of Chemical and Biological Engineering, Gachon University, Seongnam-si 13120, Republic of Korea*

[5]*Department of Nuclear Science and Engineering, Massachusetts Institute of Technology, Cambridge, Massachusetts 02139, United States*

[6]*Department of Materials Science and Engineering, Massachusetts Institute of Technology, Cambridge, Massachusetts 02139, United States*

Table of contents

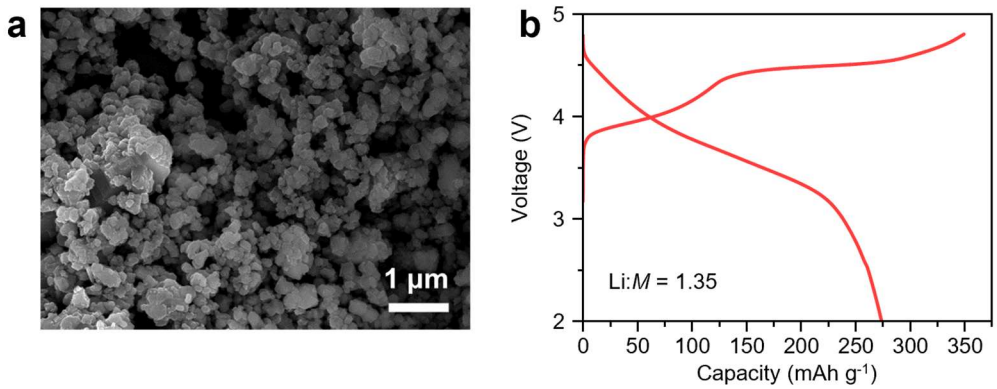

Figure S1 | Characterizations of Li under-stoichiometric LMR. (a) SEM image of LMR synthesized under a Li-deficient condition (Li/*M* = 1.35). (b) The first-cycle voltage profile of LMR synthesized at Li/*M* = 1.35. The cell was tested at 0.1 C (1 C defined as 250 mA g^{-1}) and 30 °C.

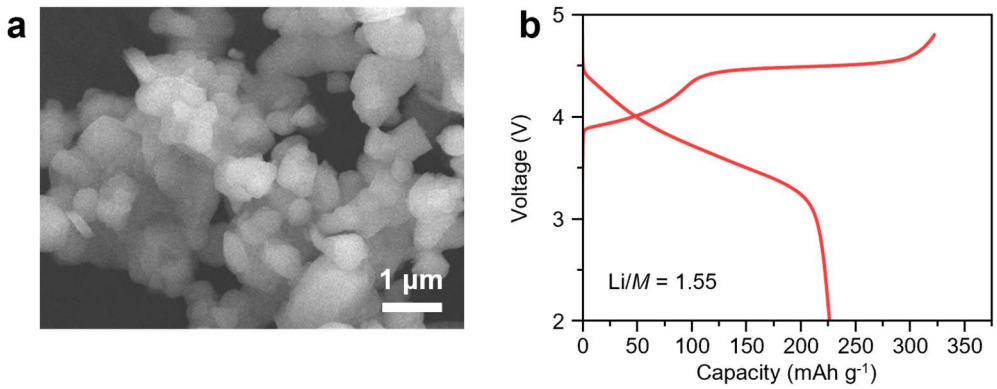

Figure S2 | Characterizations of Li over-stoichiometric LMR. (a) SEM image of LMR synthesized under a Li-excess condition (Li/*M* = 1.55). (b) The first-cycle voltage profile of LMR synthesized at Li/*M* = 1.55. The cell was tested at 0.1 C (1 C defined as 250 mA g^{-1}) and 30 °C.

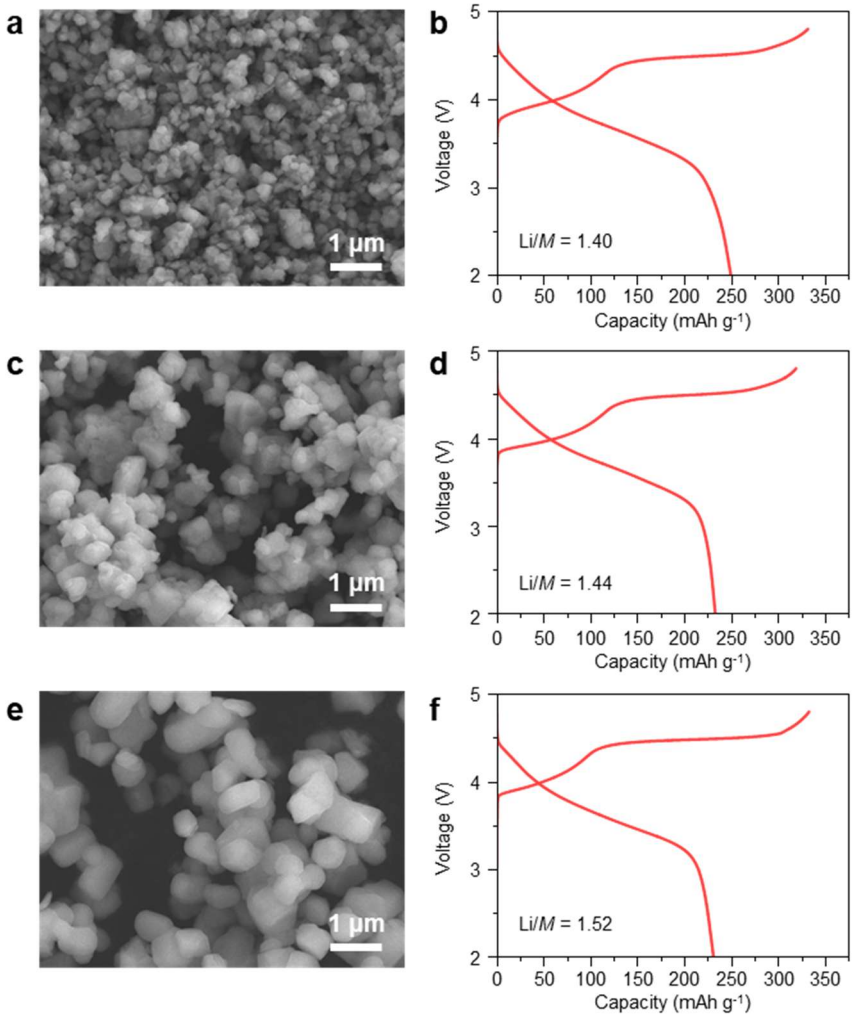

Figure S3 | Characterizations of LMR with various compositions. (a) SEM image of LMR synthesized under Li/*M* = 1.40. (b) The first-cycle voltage profile of LMR synthesized at Li/*M* = 1.40. (c) SEM image of LMR synthesized under Li/*M* = 1.44. (d) The first-cycle voltage profile of LMR synthesized at Li/*M* = 1.44. (e) SEM image of LMR synthesized under Li/*M* = 1.52. (f) The first-cycle voltage profile of LMR synthesized at Li/*M* = 1.52. The cells were tested at 0.1 C (1 C defined as 250 mA g^{-1}) and 30 °C.

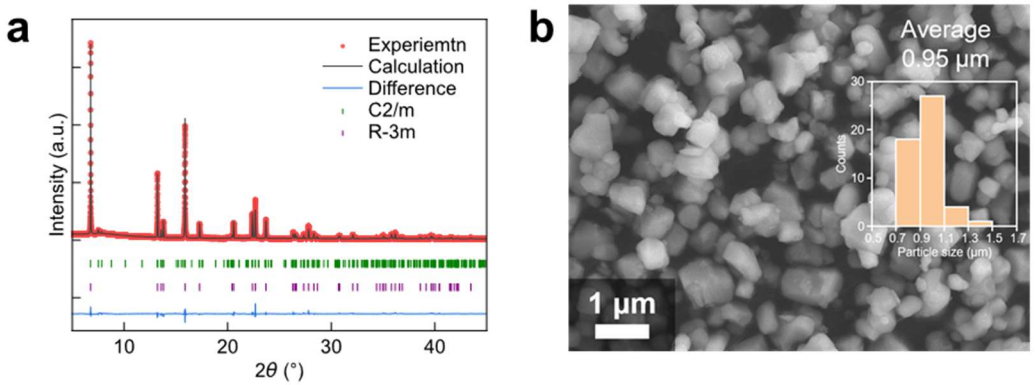

Figure S4 | Structure of SCLMR. (a) SXRD pattern of SCLMR. (b) SEM image of SCLMR (Li/*M* = 1.48).

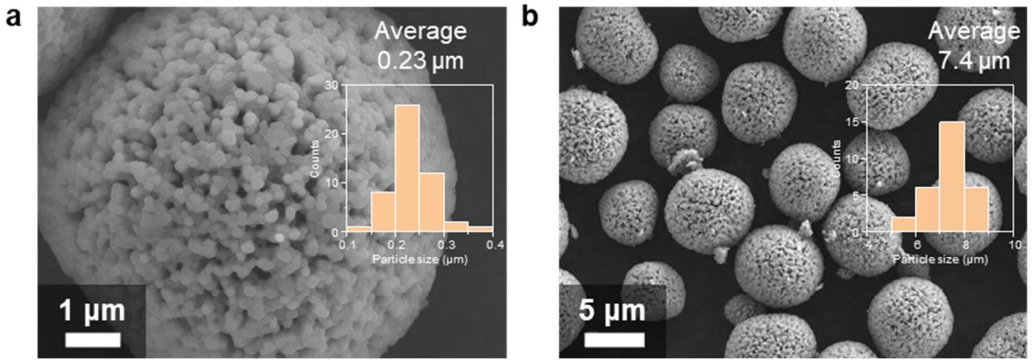

Figure S5 | Particle structure of PCLMR. (a) SEM image of PCLMR at high magnitude. Inset: primary particle size distribution. (b) SEM image of PCLMR at low magnitude. Inset: secondary particle size distribution.

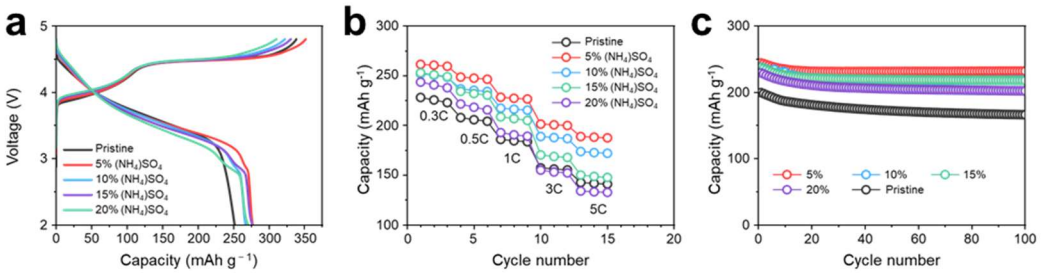

Figure S6 | Optimization of $(NH_4)_2SO_4$ amount. Using 5 wt% $(NH_4)_2SO_4$ of SCLMR, the leached SCLMR shows highest capacity (a), best rate performance (b) and highest capacity retention after 100 cycles (c). The cells were tested at 0.1 C (1 C defined as 250 mA g^{-1}) and 30 °C.

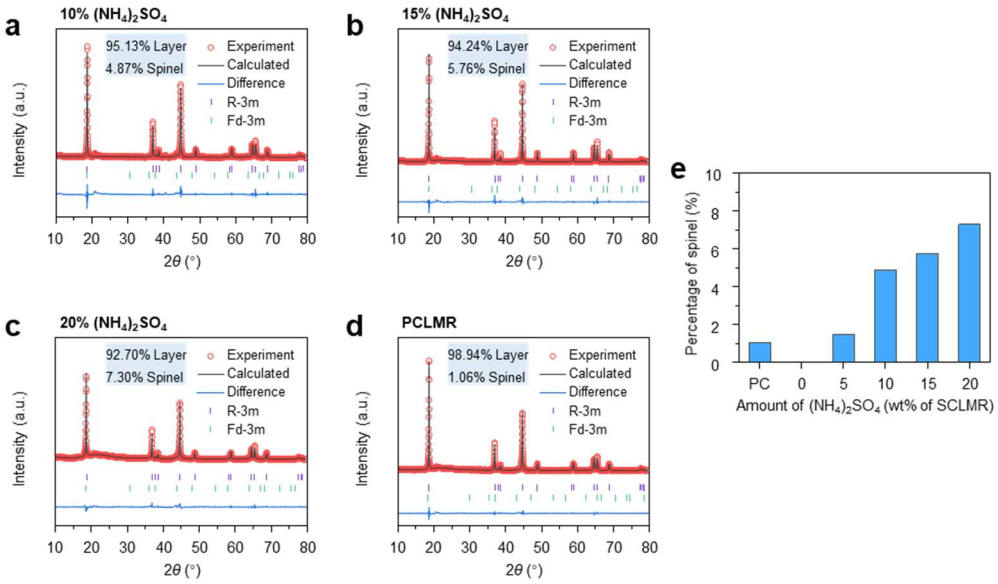

Figure S7 | XRD patterns of SCLMR leached by 10% $(NH_4)_2SO_4$ (a), 15% $(NH_4)_2SO_4$ (b), 20% $(NH_4)_2SO_4$ (c) and PCLMR (d). (e) Weight percentages of spinel phase in the samples.

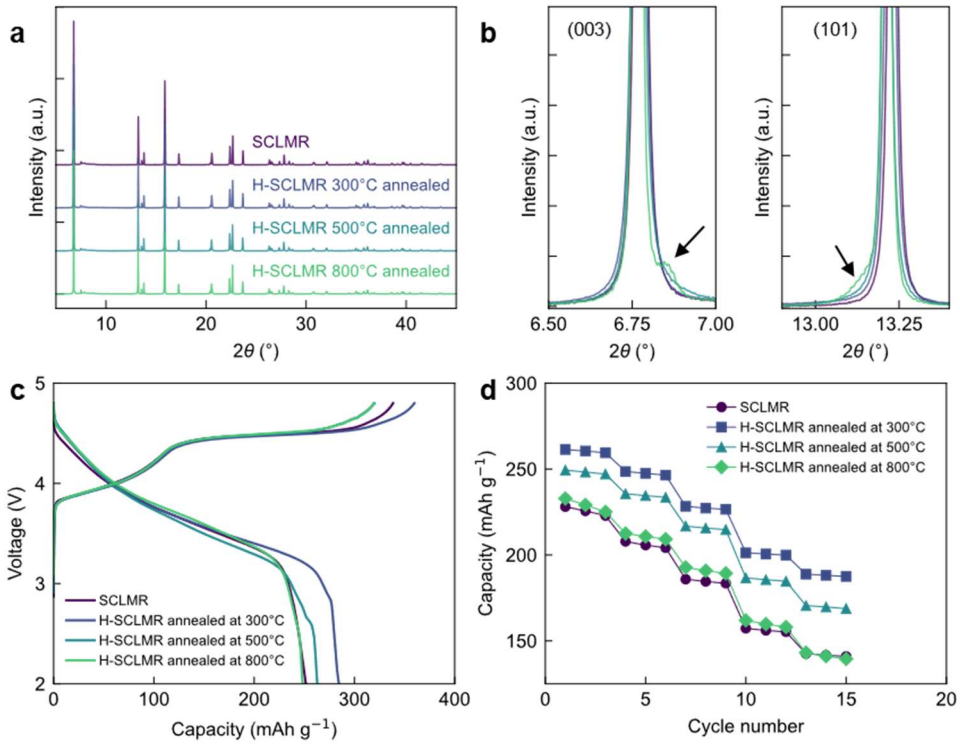

Figure S8 | Characterizations of H-SCLMR under different annealing temperature. (a) High-resolution SXRD of SCLMR and H-SCLMR annealed at 300, 500 and 800℃ (λ = 0.56025 Å). (b) Enlarged view of the 2θ region of 12.4°-13.4°. (c) Initial charge/discharge voltage profiles of SCLMR and H-SCLMR at different temperatures. The cells were tested at 0.1 C (1 C defined as 250 mA g^{-1}) and 30 °C. (d) Rate performance of SCLMR and H-SCLMR at different temperatures. The cells were tested at and 30 °C.

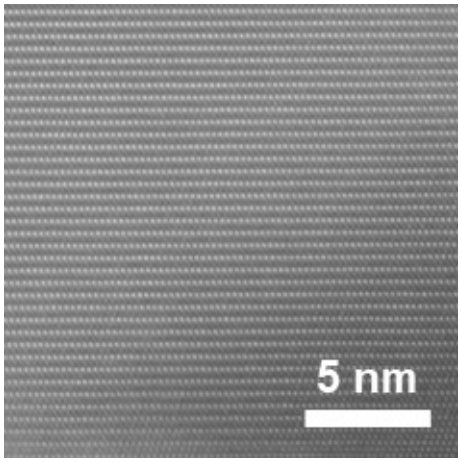

Figure S9 | HAADF-STEM image of the particle bulk in H-SCLMR. The image was taken along the [100] direction of the layered phase (with $R\bar{3}m$ space group).

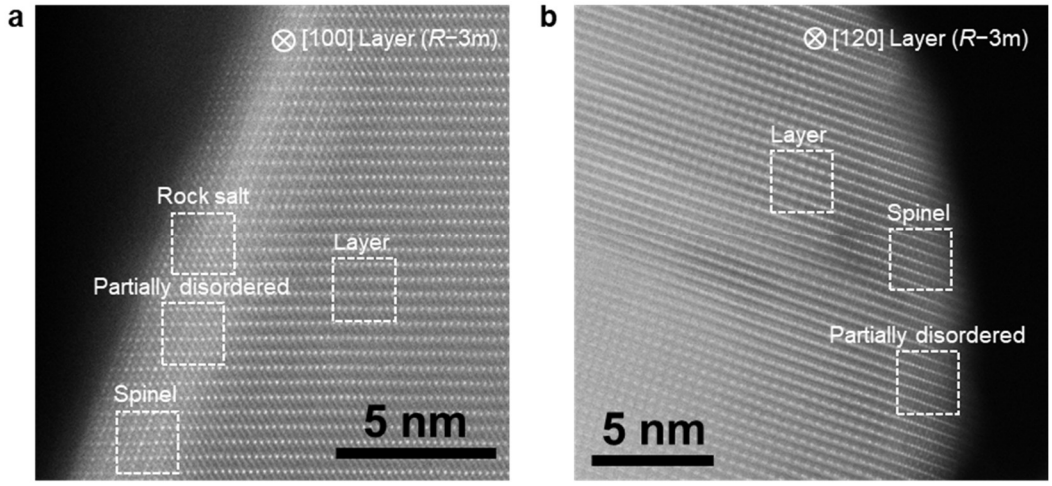

Figure S10 | STEM images of H-SCLMR at various particles and along various projections. (a) Layer [100]. (b) Layer [120].

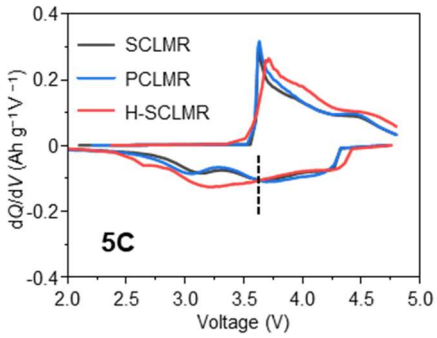

Figure S11 | *dQ*/*dV* plot at 5 C/5 C (1 C defined as 250 mA g^{-1}) charge/discharge. The data were derived from the 14th cycle in Figure 2b.

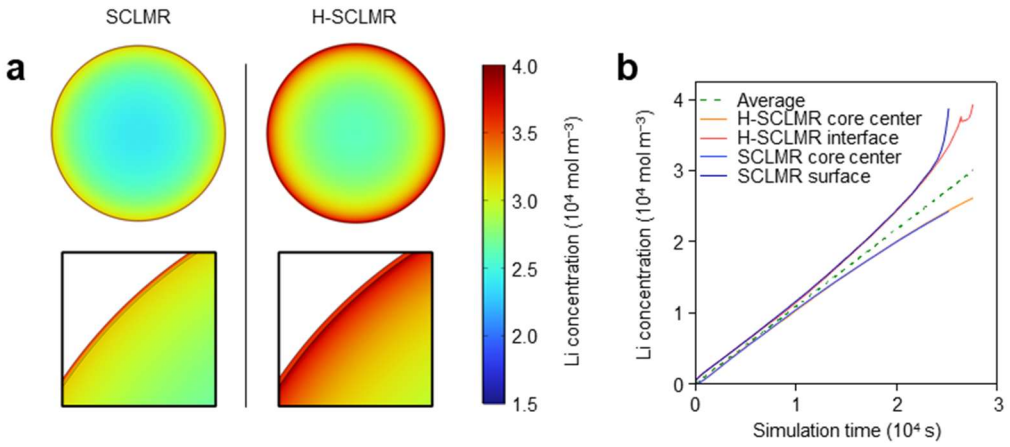

Figure S12 | FEA simulation results. (a) Simulated Li concentration distributions of SCLMR and H-SCLMR at the fully discharged state. (b) Li concentration at various points as functions of simulation time.

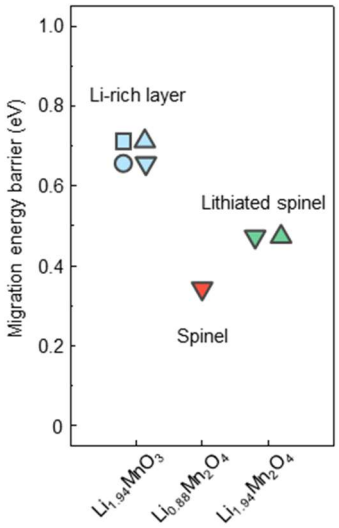

Figure S13 | Comparison of Li^+ migration energy barriers.

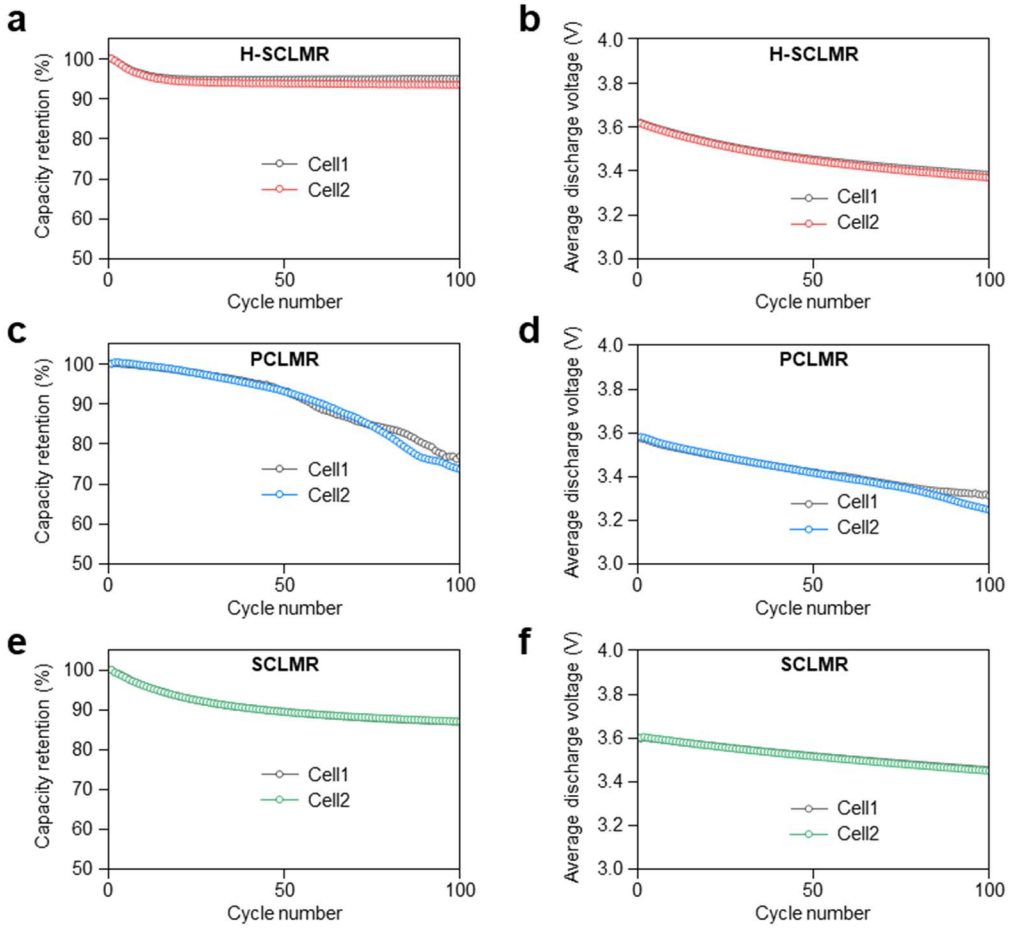

Figure S14 | Validation of cycling performance. Capacity retention (a, c, e) and average discharge voltage (b, d, f) of H-SCLMR (a, b), PCLMR (c, d) and SCLMR (e, f). All the data were collected from coin cells at 0.5 C (1 C defined as 250 mA g^{-1}) and 30 °C..

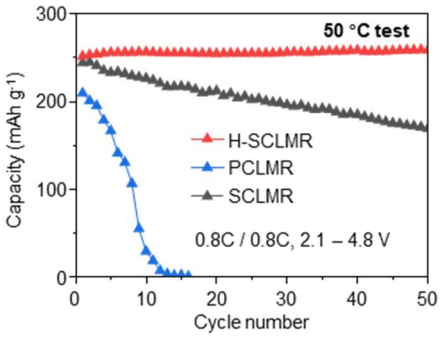

Figure S15 | Cycling performance at 0.8 C/0.8 C (1 C defined as 250 mA g^{-1}) charge/discharge between 2.1-4.8 V (vs. Li^+/Li) at 50°C.

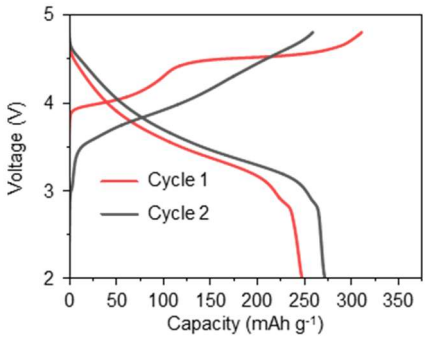

Figure S16 | The formation cycles of the single-layer pouch cell. The cell was tested at 0.1 C (1 C defined as 250 mA g^{-1}) and 25 °C.

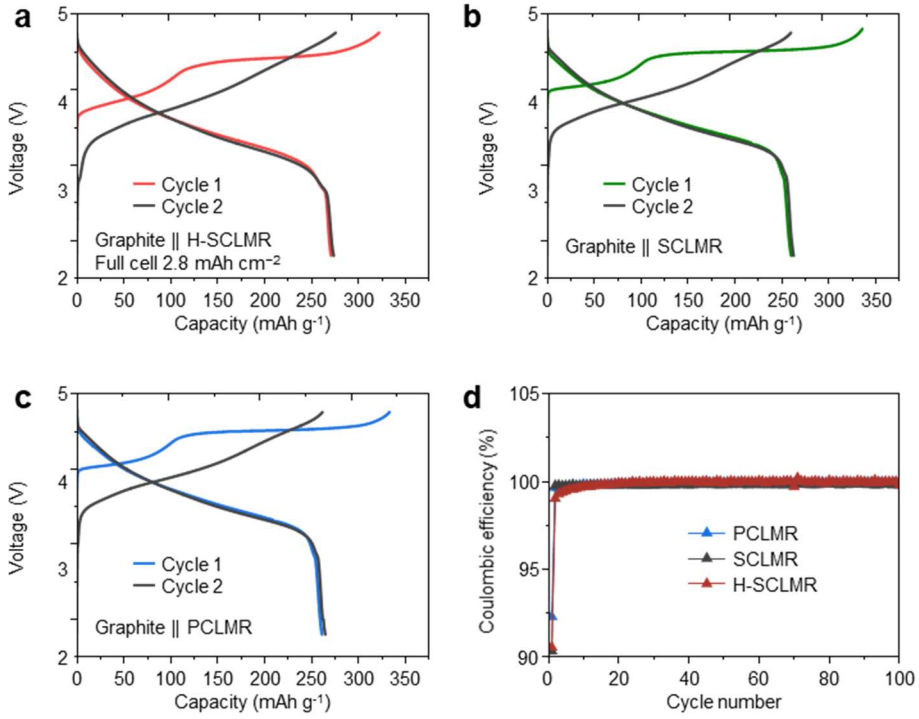

Figure S17 | Full cell performance. (a) Voltage profiles of the first two formation cycles of the graphite || H-SCLMR full cell. The rate is 0.1 C based on the mass of positive electrode materials. (b) Voltage profiles of the first two formation cycles of the graphite || SCLMR full cell. The rate is 0.1 C based on the mass of positive electrode materials. (c) Voltage profiles of the first two formation cycles of the graphite || PCLMR full cell. The rate is 0.1 C based on the mass of positive electrode materials. (d) Coulombic efficiency evolution of the full cell during cycling. The cycling rate is 0.2 C charge/0.5 C discharge (1 C defined as 250 mA g^{-1}). The cells were tested at 30 °C.

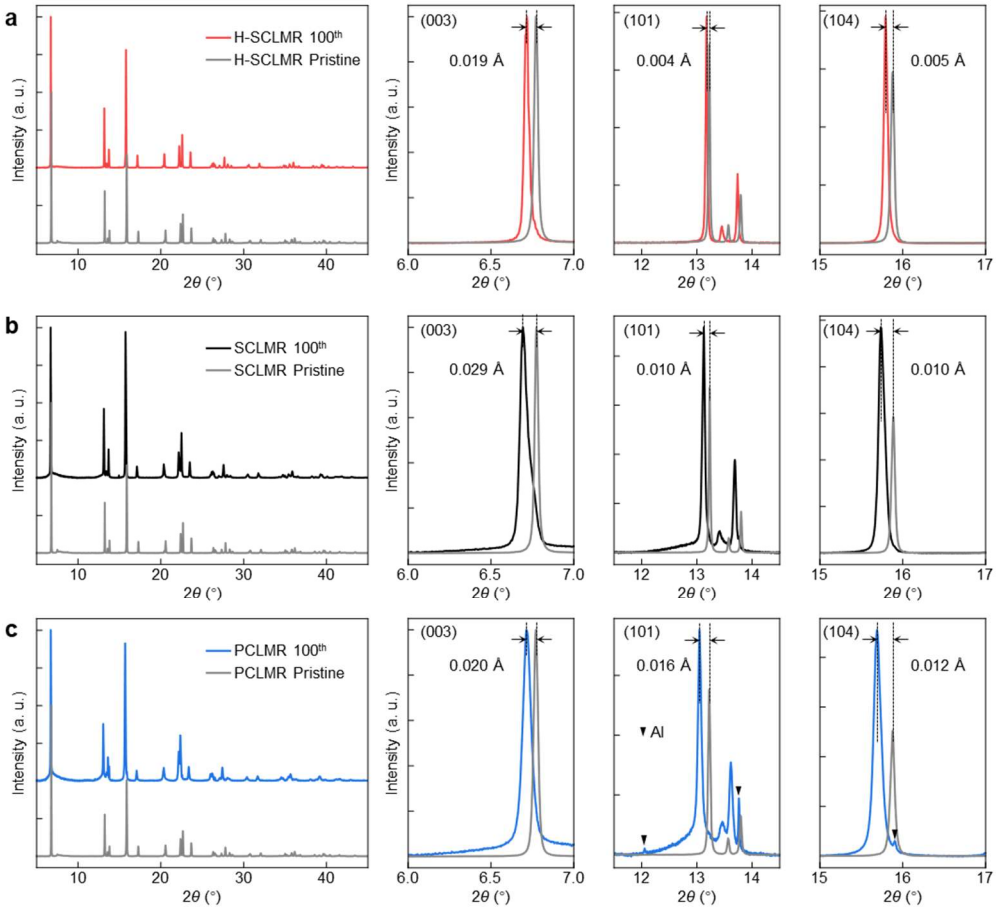

Figure S18 | SXRD of LMRs before and after long-term cycling. (a) SXRD patterns of H-SCLMR at the pristine state and after 100 cycles. Enlarged views of layer (003), (101) and (104) peaks were shown. (b) SXRD patterns of SCLMR at the pristine state and after 100 cycles. Enlarged views of layer (003), (101) and (104) peaks were shown. (c) SXRD patterns of PCLMR at the pristine state and after 100 cycles. Enlarged views of layer (003), (101) and (104) peaks were shown.

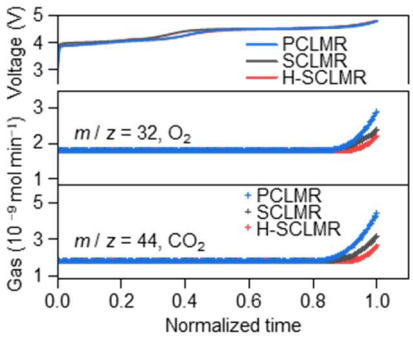

Figure S19 | Gases evolution of PCLMR, SCLMR and H-SCLMR measured by DEMS during the first charge.

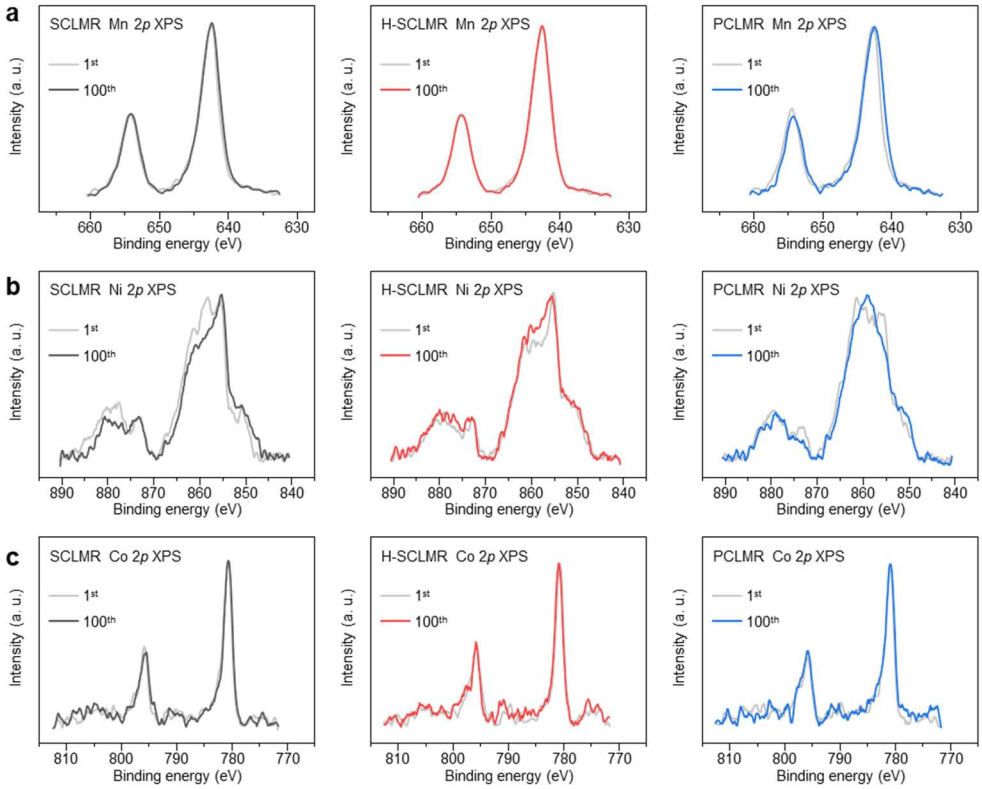

Figure S20 | XPS results of LMRs before and after long-term cycling. (a) Mn 2*p* XPS of SCLMR, H-SCLMR and PCLMR at the pristine state and after 100 cycles. (b) Ni 2*p* XPS of SCLMR, H-SCLMR and PCLMR at the pristine state and after 100 cycles. (c) Co 2*p* XPS of SCLMR, H-SCLMR and PCLMR at the pristine state and after 100 cycles.

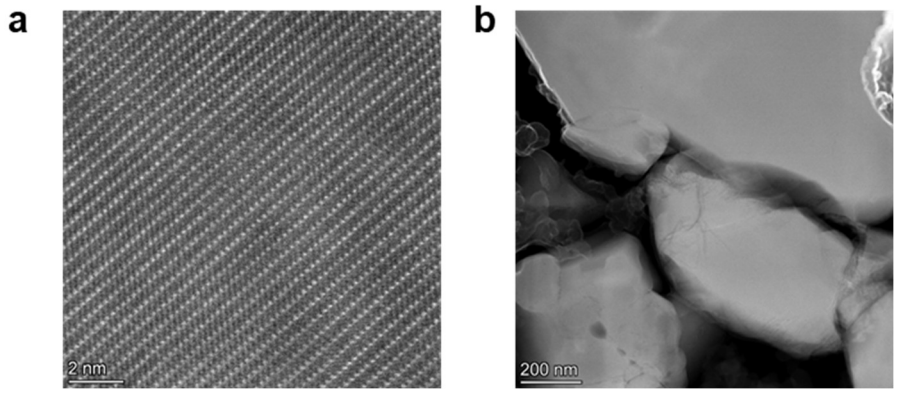

Figure S21 | Post-cycling STEM results of H-SCLMR. (a) Particle bulk STEM image of cycled H-SCLMR. (b) STEM image of cycled H-SCLMR electrode in a lower magnitude.

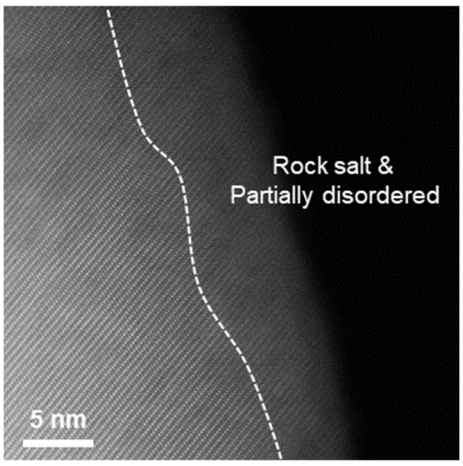

Figure S22 | Surface STEM image of SCLMR after 150 cycles.

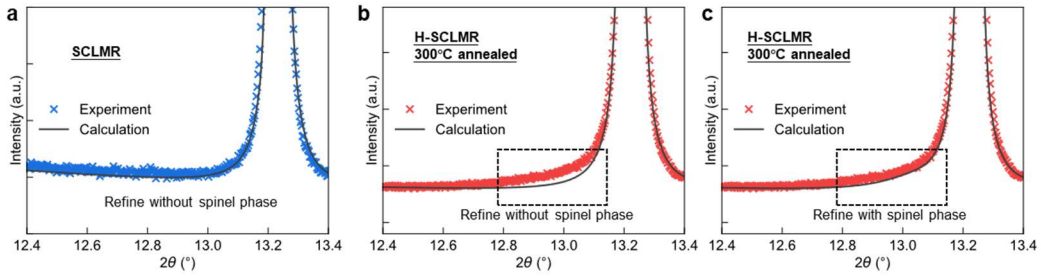

Figure S23 | Rietveld refinement results at the 2θ region of 12.4°-13.4°. (a) SCLMR. (b) H-SCLMR without including a spinel phase. (c) H-SCLMR including a spinel phase.

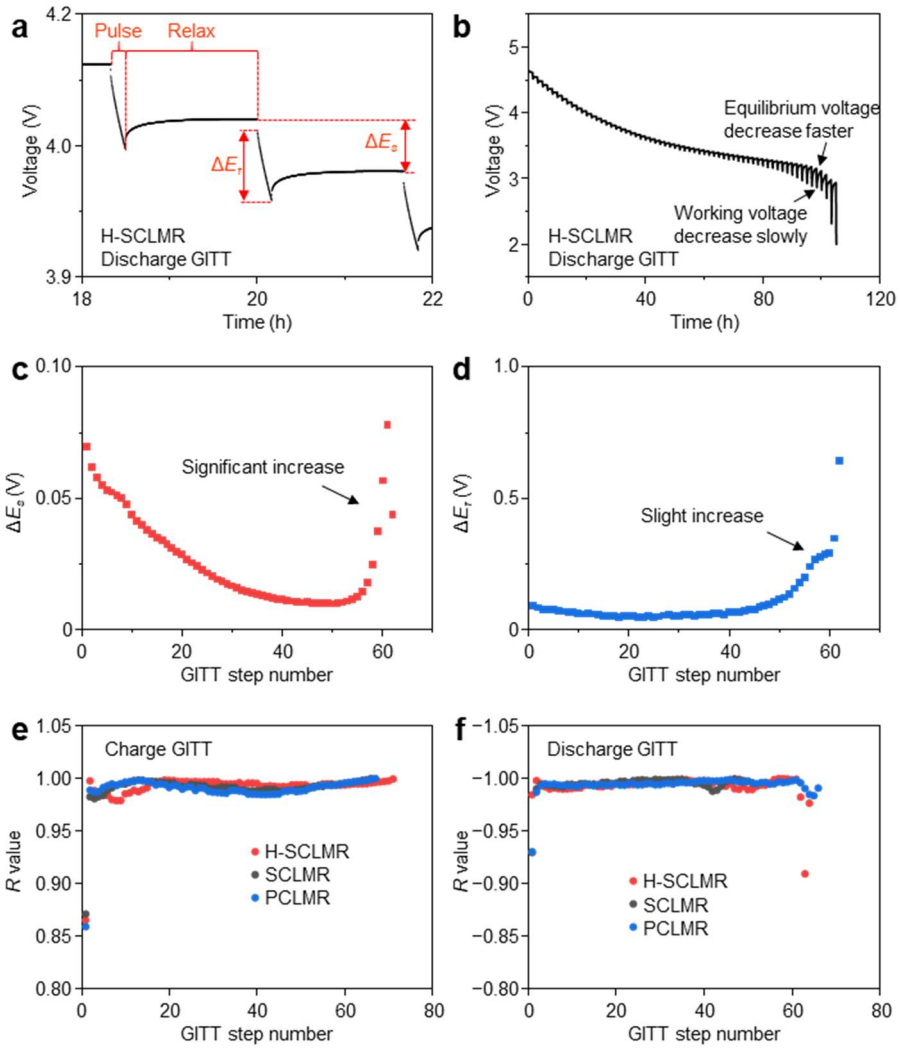

Figure S24 | In-depth analysis of GITT results. (a) Schematic explanation of ΔE_s and ΔE_τ in a typical GITT step. (b) Voltage profile of discharge GITT of H-SCLMR. (c) ΔE_s evolution during the discharge GITT test. (d) ΔE_τ evolution during the discharge GITT test. (e) R values of the linear fitting between E and the square root of t during the current pulse steps in charge GITT test. (f) R values of the linear fitting between E and the square root of t during the current pulse steps in discharge GITT test.

Table S1 | Crystallographic data of SCLMR obtained from Rietveld refinement of SXRD pattern

Sample: SCLMR. Agreement factors: R_{wp} = 6.53%.						
Phase 1 Space group: *R*−*3m*	*a* = *b* = 2.849(6) Å, *c* = 14.21(8) Å, *V* = 99.99(0) Å^3. Weight fraction = 77.3%					
	Atom	Site	*x*/*a*	*y*/*b*	*z*/*c*	Occupancy
	Li1	3*b*	0	0	0.5	1
	Mn1	3*a*	0	0	0	0.666
	Co1	3*a*	0	0	0	0.167
	Ni1	3*a*	0	0	0	0.167
	O1	6*c*	0	0	0.259	1
Phase 2 Space group: *C2/m*	*a* = 4.938(1) Å, *b* = 8.549(7) Å, *c* = 5.017(9) Å, *V* = 200.3(0) Å^3. *α* = *γ* = 90°, *β* = 109.0(0)°. Weight fraction = 22.7%					
	Atom	Site	*x*/*a*	*y*/*b*	*z*/*c*	Occupancy
	Li1	4*h*	0	0.339	0.5	1
	Li2	2*c*	0	0	0.5	1
	Li3	2*b*	0	0.5	0	1
	Ni1	4*g*	0	0.167	0	0.167
	Co1	4*g*	0	0.167	0	0.167
	Mn1	8*j*	0	0.167	0	0.666
	O1	4*i*	0.248	0.172	0.771	1
	O2	4*i*	0.250	0	0.221	1

Table S2 | Chemical composition of the samples measured by ICP-OES.

Sample	Composition
SCLMR	$Li_{1.18}Mn_{0.50}Ni_{0.15}Co_{0.17}O_2$
PCLMR	$Li_{1.17}Mn_{0.50}Ni_{0.16}Co_{0.17}O_2$
H-SCLMR	$Li_{1.16}Mn_{0.51}Ni_{0.16}Co_{0.17}O_2$

Table S3 | Specific surface area of the sample.

Sample	Specific surface area (m^2 g^{-1})
SCLMR	4.464
PCLMR	6.760
H-SCLMR	4.488

Table S4 | Crystallographic data of H-SCLMR obtained from Rietveld refinement of SXRD pattern using a 3-phase model.

Sample: H-SCLMR. Agreement factors: R_{wp} = 7.52%.						
Phase 1 Space group: *R−3m*	$a = b$ = 2.851(1) Å, c = 14.22(6) Å, V = 100.1(5) Å^3. Weight fraction = 73.1%					
	Atom	Site	*x*/*a*	*y*/*b*	*z*/*c*	Occupancy
	Li1	3*b*	0	0	0.5	1
	Mn1	3*a*	0	0	0	0.666
	Co1	3*a*	0	0	0	0.167
	Ni1	3*a*	0	0	0	0.167
	O1	6*c*	0	0	0.259	1
Phase 2 Space group: *C2/m*	a = 4.938(9) Å, b = 8.549(6) Å, c = 5.026(7) Å, V = 200.3(3) Å^3. $\alpha = \gamma = 90°$, β = 109.3(0)°. Weight fraction = 25.4%					
	Atom	Site	*x*/*a*	*y*/*b*	*z*/*c*	Occupancy
	Li1	4*h*	0	0.339	0.5	1
	Li2	2*c*	0	0	0.5	1
	Li3	2*b*	0	0.5	0	1
	Ni1	4*g*	0	0.167	0	0.167
	Co1	4*g*	0	0.167	0	0.167
	Mn1	8*j*	0	0.167	0	0.666
	O1	4*i*	0.248	0.172	0.771	1
	O2	4*i*	0.250	0	0.221	1
Phase 3 Space group: *Fd−3m*	$a = b = c$ = 8.185(9) Å, V = 548.5(3) Å^3. $\alpha = \beta = \gamma = 90°$. Weight fraction = 1.5%					
	Atom	Site	*x*/*a*	*y*/*b*	*z*/*c*	Occupancy
	Li1	8*b*	0.125	0.125	0.125	1
	Ni1	16*c*	0.5	0.5	0.5	0.167
	Co1	16*c*	0.5	0.5	0.5	0.167
	Mn1	16*c*	0.5	0.5	0.5	0.666
	O1	32*e*	0.263	0.263	0.263	1

Supplementary Note 1 | Necessity of an additional spinel phase in SXRD refinements

Figure S8a presents the SXRD patterns of pristine SCLMR, H-SCLMR, and H-SCLMR subjected to annealing at elevated temperatures, while **Figure S8b** shows an enlarged view of the relevant 2θ region of interest. In H-SCLMR, an additional diffraction signal is observed slightly below the (101) reflection of the layered phase. As the crystallinity of the secondary phase increases upon thermal annealing, this weak signal gradually evolves into a discernible diffraction peak, indicating that it originates from a structurally distinct phase rather than noise or background fluctuation. Notably, similar diffraction features associated with surface-derived spinel-like phases have been reported in previous studies, supporting our assignment of this signal to a spinel-related structure.

Furthermore, Rietveld refinements were carried out for both SCLMR and H-SCLMR. For pristine SCLMR, a satisfactory agreement between calculated and experimental patterns near the (101) reflection can be achieved without introducing any additional spinel phase (**Figure RS22a**). In contrast, for H-SCLMR, the refinement fails to reproduce the experimental profile (**Figure S23b**) in this region unless a secondary spinel-like phase is included (**Figure S239c**). Incorporation of the spinel phase also improves the fitting quality and reduces the R_{wp} value, indicating that its introduction is not arbitrary but required to accurately describe the experimental data.

Supplementary Note 2 | Origin of anomalous D_{Li} of H-SCLMR at the end-of-discharge period

GITT applies a small constant current pulse for a short time (τ), driving the cell away from equilibrium, followed by a long relaxation period to reach a new equilibrium. By analyzing the voltage transient during the pulse, we can estimate D_{Li}.
For a spherical particle model, the most cited equation is:

Equation S1: The Fundamental GITT Diffusion Formula

$$D_{\mathrm{Li}} = \frac{4}{\pi\tau}\left(\frac{n_m V_m}{A}\right)^2\left(\frac{\Delta E_S}{\Delta E_\tau}\right)^2$$

Where:
D_{Li}: Chemical diffusion coefficient of Li^+ in the electrode (cm^2/s)
τ: Duration of the constant current pulse (s)
n_m: Molar number of the active material in the electrode (mol)
V_m: Molar volume of the active material (cm^3/mol)
A: Electrode/electrolyte interfacial area (cm^2). Often approximated as the total surface area of active particles.
ΔE_s: The steady-state voltage change due to the current pulse. This is the difference between the OCV before the pulse and the OCV after full relaxation.
ΔE_τ: The total voltage change during the current pulse, excluding the initial instantaneous IR drop.

Figure S23a shows a schematic explanation of ΔE_s and ΔE_τ.
If we know the particle radius (r), assume spherical particles:
$A = (3n_mV_m) / r$ (since Total Volume = n_mV_m, and Area/Volume for a sphere = $3/r$).
Substituting this into **Equation S1** simplifies it to the most usable form:

$$D_{\mathrm{Li}} = \frac{4}{\pi\tau}\left(\frac{r}{3}\right)^2\left(\frac{\Delta E_S}{\Delta E_\tau}\right)^2$$

This means if τ is controlled to be the same for each step, D_{Li} is proportional to $(\Delta E_s / \Delta E_\tau)^2$. From their definition, we know that ΔE_s is highly correlated to the equilibrium voltage change and ΔE_τ is approximately equal to $\Delta E_s + \delta$ (δ represent overpotential).
Figure S23b shows the voltage profile of discharge GITT of H-SCLMR. **Figure S23c** and **S23d** show the evolution of ΔE_s and ΔE_τ obtained during the discharge GITT test of H-SCLMR. At the end-of-discharge period, ΔE_s increases significantly (for clarity, ΔE_s and ΔE_τ are represented using absolute value), while ΔE_τ increases only slightly. This makes $(\Delta E_s / \Delta E_\tau)^2$ dramatically increase leading to increase of apparent D_{Li} at the end-of-discharge period.
Because ΔE_τ is approximately equal to $\Delta E_s + \delta$, these results indicate that the overpotential decrease during this period. We can therefore simplistically understand that the increase of apparent D_{Li} is caused by the decrease of overpotential.
The decrease of overpotential can be explained by the low-voltage lithiation activity of surface phases. As proved by the finite element analysis results, the surface spinel phase could release extended capacity. At this plateau region, the equilibrium voltage continuously drops because the

bulk is being continuously lithiated. However, the working voltage remains largely unchanged at the plateau, which makes the difference between equilibrium voltage and working voltage lower, which, in other word, presents decreased overpotential.

In conclusion, the anomalous increase of the apparent Li^+ diffusion coefficient (D_{Li}) originates from the buffering effect of the surface phases. The ionically conductive and electrochemically active surface structure promotes more homogeneous lithiation, thereby reducing the gap between the equilibrium and working voltages. This effectively suppresses polarization, lowers the overpotential, and ultimately manifests as an increased apparent D_{Li}.

Supplementary Note 3 | The condition of potential-concentration linearity in diffusion coefficient calculations

To validate diffusion coefficient calculations, the condition of potential-concentration linearity during the electrochemical experiments must be demonstrated. The derivations of GITT method start from solving the equations describing Fick's second law.

$$\frac{\partial C(r,t)}{\partial t} = D\frac{\partial^2 C(r,t)}{\partial r^2}$$

where C is the concentration of the diffusing species, r is the radial distance in the spherical coordinates, t is time and D is the diffusion coefficient. The boundary conditions with an applied current $i(t)$ and an initial concentration C_0 are as follows:

$$\begin{cases} -D\dfrac{\partial^2 C(r,t)}{\partial r^2} = \dfrac{i(t)}{nFA} \\ C(r,0) = C_0 \end{cases}$$

Where r_p is the radius of the electrode particle, n is the charge number of the diffusing species (which is 1 for Li^+), F is the Faraday constant and A is the area of the surface where the diffusing ions enter the electrode material. For the GITT, a constant current I is applied.

$$i(t) = I$$

The full solution details can be found in Ref.1. When $t << r_p^2/D$, semi-infinite diffusion can be assumed. In our cases, the lowest r_p^2/D can be evaluated by the radius of single-crystal particle (~0.5 μm) and the maximum D_{Li} value in **Figure 2d** (~$10^{-13.5}$ cm^2 s^{-1}) to be 7.9×10^4 s, which is much greater than the pulse time (6×10^2 s). Thus, the concentration at the surface C_s can be expressed as:

$$C_s(t) = C(r_p,t) = C_0 - \frac{2I\sqrt{t}}{FA\sqrt{D\pi}}$$

It can be seen that C_s is linearly related to the square root of t. Therefore, to verify the linear relationship between E and C_s, it is only necessary to verify the linear relationship between E and the square root of t. During GITT measurements, both the potential (E) during pulse charge/discharge and time (t) can be measured in real time, so the linearity can be verified by calculating the R-value of the linear fit between E and the square root of t.

The R-values obtained from linear fitting of each GITT step show that for the charge/discharge processes of all three materials, only few data points at the very beginning or very end of the charge/discharge exhibits a low R-value (**Figure S23e** and **S23f**). For the remaining data points, the absolute R-values are greater than 0.95, with most exceeding 0.98. Therefore, it can be concluded that the potential-concentration linearity holds. More importantly, even if these non-linear points are disregarded, the conclusions drawn in our paper remain unaffected.

References

1 Chien, YC., Liu, H., Menon, A.S. *et al.* Rapid determination of solid-state diffusion coefficients in Li-based batteries via intermittent current interruption method. *Nat Commun* **14**, 2289 (2023). https://doi.org/10.1038/s41467-023-37989-6